Near Infrared Optical Manipulation of a GaAs/AlGaAs Quantum Well in the Quantum Hall Regime

Jonathan M. Buset

Department of Physics
McGill University
Montréal, Québec, Canada
August 2008

A thesis submitted to McGill University
in partial fulfilment of the requirements of the degree of
Master of Science

To my parents.
For always encouraging me to follow my dreams.

Abstract

Using electronic spin rather than charge to replace existing microelectronic systems has been a well studied area of research in the last ten years. More recently, research has focused on using the nuclear spin of GaAs rather than the electron spin. This work has demonstrated that GaAs nuclear spins have many desirable properties and show great potential as quantum information carriers. The challenge in the implementation of nuclear spins lies in the ability to control and retrieve the information that they carry. One proposed method is to dynamically polarize the GaAs nuclear spins using circularly polarized photoexcitation. If successful, this could open new horizons in the field of quantum information processing.

This thesis details an investigation into the use of polarized light to manipulate the properties of a GaAs/AlGaAs quantum well sample. The three main topics explored in this thesis are: 1) the design and operation of a polarization controller that is able to shine well-defined and tunable polarized light on to a sample contained in a cryogenic environment at $T = 0.27\,\mathrm{K}$; 2) the manipulation of the nuclear polarization in GaAs using low power laser light with tunable polarization; and 3) a preliminary investigation into illuminating a quantum Hall sample with unfocused, low power laser light and the transport properties modifications that occur in the quantum Hall regime.

Résumé

L'utilisation du spin électronique plutôt que la charge électronique pour remplacer les systèmes microélectroniques a été un domaine bien étudié de la recherche au cours des dix dernières années. Plus récemment, la recherche a porté sur l'utilisation du spin nucléaire du GaAs plutôt que le spin électronique. Ce travail a démontré que les spins nucléaires du GaAs ont de nombreuses propriétés désirables et montrent un grand potentiel en tant que transporteurs de l'information quantique. Le défi dans la mise en œuvre des spins nucléaires réside dans la capacité de contrôler et de récupérer les informations qu'elles transportent. Une méthode proposée consiste à polariser dynamiquement les spins nucléaires du GaAs en utilisant la photoexcitation polarisée circulairement. Ceci pourrait ouvrir de nouveaux horizons dans le domaine du traitement de l'information quantique.

Cette thèse expose en détails une enquête sur l'utilisation de la lumière polarisée pour manipuler les propriétés d'un échantillon puit quantique de GaAs/AlGaAs. Les trois principaux sujets abordés dans cette thèse sont les suivants: 1) la conception et le fonctionnement d'un contrôleur de polarisation qui est capable d'émettre une lumière polarisée bien définie et ajustable sur un échantillon dans un environnement cryogénique à $T = 0.27\,\mathrm{K}$, 2) la manipulation de la polarisation nucléaire dans le GaAs en utilisant un laser à faible puissance avec une polarisation ajustable, et 3) une enquête préliminaire sur l'illumination d'un échantillon de Hall quantique avec

un laser non-focalisé à faible puissance et les modifications des propriétés de transport qui se produisent dans le régime de Hall quantique.

Acknowledgements

The research group that I worked in was full of fun and friendly peers, all of whom I now consider to be my friends. My heartfelt thanks go out to all of the past and present members of the Gervais Group. Immeasurable thanks go to Cory Dean and Dr. Benjamin Piot for their guidance, encouragement and support throughout the many days and long nights we spent together in the lab; to Andrew Mack for your endless enthusiasm and tireless work spent building and testing the optics system; to Dominique Laroche for preparing our sample and teaching me to use the cryogenic system; to Michel Savard for sharing our cramped corner of the basement; to James Hedberg for making the lab an amazingly fun place to work in; to Vera Sazonova for your amazing Labview skills; and to my supervisor Dr. Guillaume Gervais for providing the equipment and helium necessary to help run all of my experiments.

Many people around the Rutherford building have directly contributed to my research and I would like to acknowledge their contributions here. Thanks go out to John Smeros for ensuring that the liquid helium was always plentiful; to Richard Talbot for helping to build the apparatus and ensuring that everything stayed in working order; to Dr. Paul Wiseman for enlightening conversations on the Faraday rotation model; and to Dr. Thomas Szkopek for conversations regarding the phenomena discussed in Chapter 4.

I also wish to thank all of my friends in the Department of Physics for making these past two years fun and enjoyable. Many thanks go to Philip Egberts for sharing a cube with me and keeping me entertained throughout the long days; to Dylan McGuire and Jody Swift for keeping me fed and well caffeinated throughout this entire process; to Adam Schneider for always being around to have a chat with; to Étienne Marcotte for being my go-to guy for everything Matlab, to Jeff Bates and Jessica Topple for being amazing neighbours; and to the rest of my friends in the department: Tobin Filleter, Jesse Maassen, Chris Voyer, René Breton, Aleks Labuda, Dan O'Donnell, Kevin MacDermid, James Kennedy, Vance Morrison, Robert Chatelain, and Ashley Faloon. Sincere apologies to anyone that I may have forgotten.

Throughout many of the long days and nights spent completing this work, I have been supported by my wonderful girlfriend Jessica. Her patience and kindness during this process has been above and beyond the call of duty.

Finally, I wish to thank my family for always supporting me in whatever (mis)-adventures I get myself into. Immeasurable thanks go to my parents Richard and Liz; to my grandparents; to my sister Kathleen; and to all of my extended family. This whole process would not have been possible without your love and support.

Table of Contents

List of Figures

List of Abbreviations

2DEG . . . . Two-Dimensional Electron Gas

DNP . . . . Dynamic Nuclear Polarization

FQHE . . . . Fractional Quantum Hall Effect

IQHE . . . . Integer Quantum Hall Effect

LED . . . . Light Emitting Diode

MBE . . . . Molecular Beam Epitaxy

MOSFET . . . . Metal-Oxide Semiconductor Field Effect Transistor

NMR . . . . Nuclear Magnetic Resonance

NPC . . . . Negative Photoconductivity

NPPC . . . . Negative Persistent Photoconductivity

OPNMR . . . . Optically Pumped Nuclear Magnetic Resonance

PPPC . . . . Positive Persistent Photoconductivity

RDNMR . . . . Resistively Detected Nuclear Magnetic Resonance

RF . . . . Radio Frequency

SOP . . . . State of Polarization

CHAPTER 1

Introduction

1.1 Motivation

Technological advancements in crystal growth, lithography and development processes over the last 30 years have allowed for great strides in the development of semiconductor devices. The most prevalent of these was the development of Silicon Metal-Oxide Semiconductor Field Effect Transistors (MOSFETs) which has revolutionized the technology industry worldwide. As these technologies have advanced and the feature sizes have reached the nanometer scale, the number of devices present on each integrated circuit has followed Moore's law, approximately doubling each year. As we begin to reach the limits of current fabrication techniques, new research has started to focus on the development of nanostructured devices that use an electron's spin rather than its charge for modern device applications [1].

The behaviour of these new "spintronic" devices is primarily dictated by the quantum mechanical interaction of electron charge and spin which show potential for the realization of an architecture for quantum information processing. This work is primarily motivated by the greater degree of freedom provided by spins and also their higher level of isolation from the environment which makes the quantum mechanical states less prone to decoherence [2]. In comparison to electronic spin, the nuclear spins of GaAs offer even greater isolation from the environment and show great potential as quantum information carriers if one can find a way to effectively *initialize*, *control* and *read out* their quantum mechanical states [3].

An important property of GaAs is the relatively strong hyperfine coupling that exists between the electron and the nuclear spin degrees of freedom which recently enabled the local study of multiple coherence of the nuclear spins by resistive methods [4]. These properties, in addition to the long nuclear spin coherence time ($\approx$ ms), make GaAs an appealing candidate for the implementation of quantum electronic devices based on hyperfine-coupled nuclear spins.

One potential route toward the addressing and efficient manipulation of the GaAs nuclear spins is through dynamic nuclear polarization and the optical Overhauser effect [5–7] where light in the near infrared spectrum with a well-defined circular polarization is used to create a large out-of-equilibrium nuclear spin polarization. Pumping nuclear spins via the optical Overhauser effect is more efficient with circular polarized illumination than with linear polarized light [8, 9]. The ability to control the polarization of the light in situ at the active device region offers, in principle, a means to manipulate the polarization of a small ensemble of nuclear spins.

This thesis presents an investigation into the the use of polarized light to manipulate the nuclear spins of GaAs along with an analysis of the custom built polarization controller used throughout the course of this research. In the remainder of this chapter, references will be made to several key areas of research which motivated this work.

1.1.1 GaAs/AlGaAs Quantum Wells

Advanced growth techniques such as molecular beam epitaxy (MBE) [10] can be used to grow crystal structures with mono-atomic layer precision and allow for the production of high purity GaAs/AlGaAs heterostructures. The lattice constants for GaAs and AlGaAs are very close providing an extremely low stress interface between the two materials. This produces systems with very long mean free path ($> 10\,\mu$m) and extremely high mobility [11, 12].

When two different semiconductors materials are grown together, they form a *heterojunction*. The material on each side of the junction is composed of different energy bandgaps resulting in an energy discontinuity at the junction interface. If the material boundary is an abrupt change, there will be a sharp energy discontinuity. Alternatively, if the material transition is gradual, the energy bandgap at the junction can be customized for different applications. In the case of a GaAs/$\mathrm{Al}_x\mathrm{Ga}_{1-x}\mathrm{As}$ heterojunction, shown in Fig. 1–1, the fraction x can be varied over a number of monolayers using advanced growth techniques to tune the slopes of the energy band.

The main difference between GaAs and $\mathrm{Al}_x\mathrm{Ga}_{1-x}\mathrm{As}$ is the conduction band energy. For example, if $x = 0.3$, the conduction band of the $Al_{0.3}Ga_{0.7}As$ will be 300 meV greater than that of GaAs. In this case, the electrons will flow from the wide-bandgap $\mathrm{Al}_x\mathrm{Ga}_{1-x}\mathrm{As}$ into the GaAs side of the junction to gain energy, and the junction will reach thermal equilibrium. For a pure semiconductor system at extremely low temperatures ($T \approx 0\,\mathrm{K}$) there will be no free carriers because the electrons follow the Fermi-Dirac probability distribution. Silicon dopants added into the AlGaAs side of the junction will provide free electrons that will move to the GaAs, taking advantage of the energy gain.

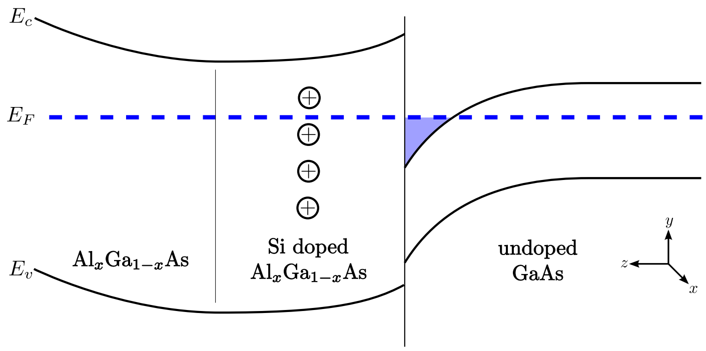

FIGURE 1–1: Example energy band diagram for a GaAs/AlGaAs heterojunction in thermal equilibrium. A mismatch of the conduction and valence band energies (E_c and E_v) of the two materials creates a potential barrier at the junction interface.

This movement of charge creates an accumulation layer of electrons in the potential well at the junction interface and a sharp discontinuity at the interface confines the electrons in the z-direction (perpendicular to the interface) but allows for their free movement in the x-y plane. This produces a condition known as a *two-dimensional electron gas* (2DEG) where the energy levels of the electrons become quantized in the z-direction. In the case of a single heterojunction, the quantum well at the interface can be approximated by a triangular potential well and the approximate energy levels of the well are depicted in Fig. 1–2 [12–15].

1.1.2 Classical Hall Effect

First discovered in 1879 [16], the Hall effect describes the motion of electrons flowing through a conducting material when placed in a perpendicular magnetic field. As each electron of charge q flows through the conductor at some velocity $\mathbf{v}$, the magnetic field $\mathbf{B}$ will exert a Lorentz force on it according to

$$\mathbf{F_m} = q\mathbf{v} \times \mathbf{B}. \tag{1.1}$$

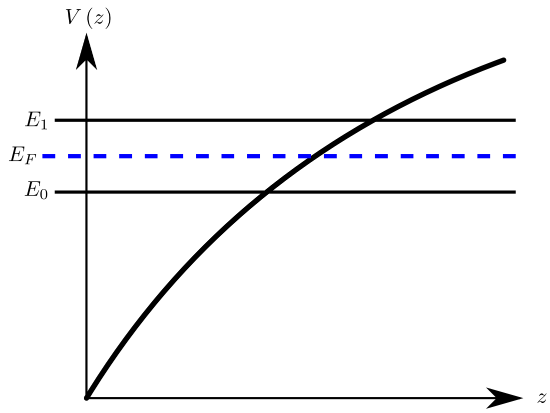

FIGURE 1–2: Triangular potential well formed by a GaAs/AlGaAs heterojunction. The resulting 2-DEG has quantized energy levels in the z-direction.

Fig. 1–3 illustrates the Hall effect in a n-type semiconductor in a uniform magnetic field $\mathbf{B} = \hat{\mathbf{z}} B_z$ with current I_x flowing in the x-direction. The electrons (or holes for p-type semiconductors) flowing through the semiconductor will undergo a force in the negative y-direction due to Eq. 1.1. The force on the carriers creates a net buildup of charge carriers on the $y = 0$ surface of the semiconductor. This buildup generates a transverse electric field in the y-direction which continues to increase until the induced field is strong enough to stop the drift of the charge carriers. Once a steady state is reached, the Lorentz force from the magnetic field will be exactly balanced by the force of the induced electric field and the net force on the charge carriers is zero.

$$\mathbf{F} = q\left[E + (\mathbf{v} \times \mathbf{B})\right] = 0 \tag{1.2a}$$

which leads to

$$qE_y = qv_xB_z. \tag{1.2b}$$

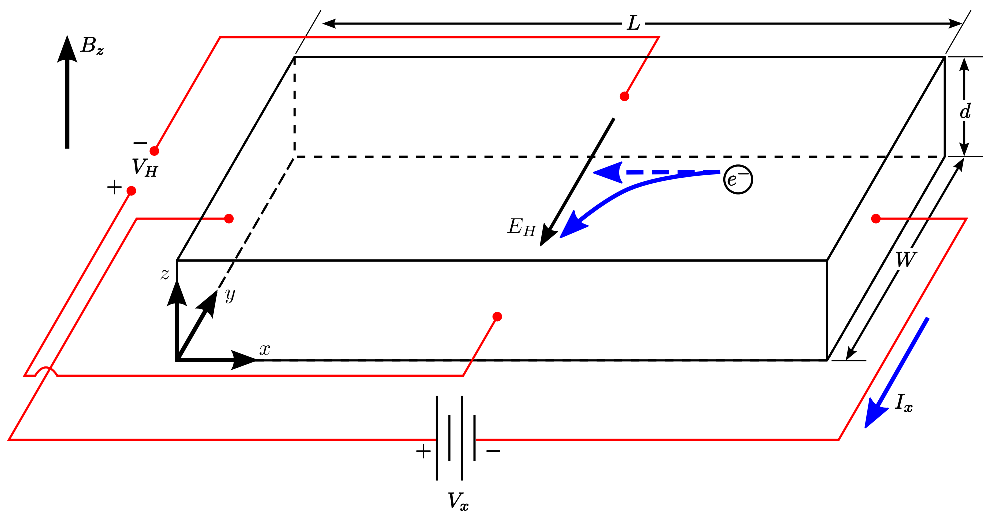

FIGURE 1–3: Illustration of the geometry used to measure the Hall effect in a n-type semiconductor.

The electric field induced in the y-direction E_H is known as the *Hall field* which produces a potential difference across the width of the semiconductor known as the *Hall voltage*. The Hall voltage in a conductor of width W is given by

$$V_H = +E_H W. \tag{1.3}$$

For metals and n-type semiconductors where electrons are the majority carrier, the induced Hall field will be in the negative y-direction and the resulting Hall voltage will be negative with the given geometry of Fig. 1–3. For the same geometry of p-type semiconductors, the induced field will be in the opposite direction and the Hall voltage will be positive. As a result, the majority carrier of an extrinsic semiconductor can be determined (either n-type or p-type) by measuring the polarity of the Hall voltage.

Combining Eq. 1.2 and Eq. 1.3, and substituting the drift velocity for electrons in a n-type semiconductor,

$$v_x = \frac{-J_x}{en} = \frac{-I_x}{(en)\,(Wd)} \tag{1.4}$$

results in a Hall voltage given by

$$V_H = -\frac{I_x B_z}{ned}. \tag{1.5}$$

Rearranging Eq. 1.5 forms a ratio known as the *Hall resistance* (also called the *Hall coefficient*).

$$R_H = \frac{V_H}{I_x} = -\frac{B_z}{ned} \tag{1.6}$$

The Hall resistance which is linear with B, proves to be a very useful tool in determining the electron density of the conducting sample [13–15, 17].

1.1.3 Integer Quantum Hall Effect

A very interesting phenomenon occurs when the Hall effect is observed in two dimensional systems held at low temperatures. When a magnetic field is applied perpendicular to the conduction plane, the in-plane motion of the carriers becomes quantized into Landau levels with energies given by

$$E_i = \left(i + \frac{1}{2}\right)\hbar\omega_c, \tag{1.7}$$

where $\omega_c = \frac{eB}{m^*}$ is the cyclotron frequency, B is the magnetic field, e is the charge of an electron and m^* is its effective mass. The number of available states per cm^2 in each Landau level,

$$d = \frac{2eB}{h}, \tag{1.8}$$

is linearly proportional to the magnetic field. At low temperatures, the Landau levels are split in two according to electron spins with each level having a degeneracy of $\frac{eB}{h}$. In this case, the electron distribution in the 2DEG is given by the Landau level filling factor

$$\nu = \frac{n}{d} = n\left(\frac{h}{eB}\right). \tag{1.9}$$

A typical transport measurement demonstrating the quantized Hall effect is shown in Fig. 1–4. As first discovered by von Klitzing, the trace exhibits the distinct plateaus in the Hall resistance and corresponding minima in magnetoresistance when the Landau level filling factor reaches integer values [18].

$$\nu = n\left(\frac{h}{eB_i}\right) = i \tag{1.10}$$

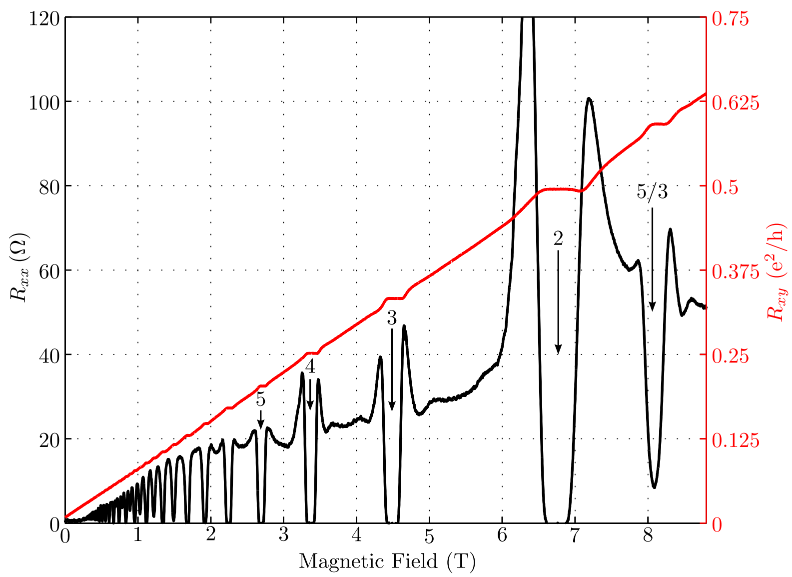

FIGURE 1–4: Example of a typical magnetotransport measurement (R_{xx} and R_{xy} vs. B) demonstrating the quantum Hall effect in a GaAs/AlGaAs 2DEG at $T \approx 270$ mK. The labelled arrows denote the Landau level filling factors ν at certain magnetic fields.

When $\nu = i$ is an integer, the Fermi energy of the system is located within one of the energy gaps and an exact number of these Landau level energy states is filled, as demonstrated in Fig. 1–5. When E_F resides within an energy gap, there are no available states for the electron to move to within the energy range of the system. The Pauli principle prohibits elastic collisions and, although inelastic collisions with phonons are possible, there are few (if any) phonons in the system with energy greater than the gap spacing. This is due to the assumption that, when a strong magnetic field is applied to the system, the energy separation will be $\hbar\omega_c \gg k_B T$, which holds true at these low temperatures. When no other energy states are available, the transport parameters (R_{xx}, R_{xy}) will assume quantized values.

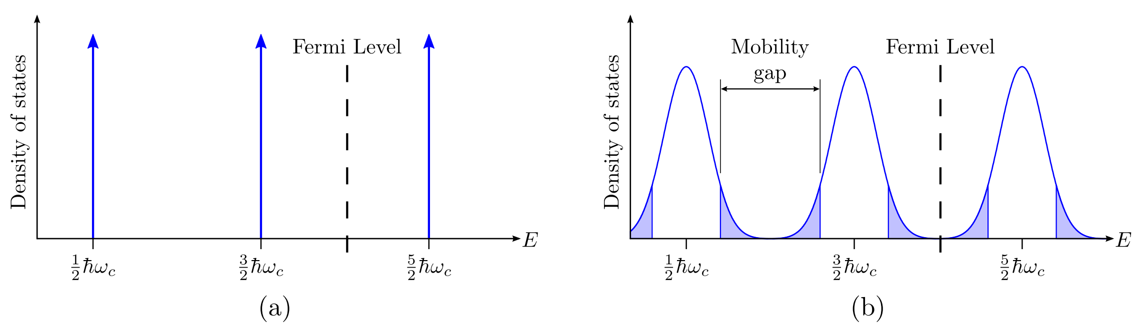

FIGURE 1–5: Density of states in a 2DEG in a strong perpendicular magnetic field. (a) An ideal 2D crystal with no disorder broadening. (b) A realistic 2D crystal where the shaded regions represent the localized states that form in the tails of each Landau level as a result of the disorder due to defects and impurities [19–21].

According to Eq. 1.10, an ideal 2D system would become quantized at exact values of B_i forming sharp δ-functions in the density of states, as illustrated in Fig. 1–5(a). For realistic systems containing impurities and disorder, the Landau levels become broadened and localized states form as a result of the residual disorder, shown in Fig. 1–5(b). As a consequence, the quantization of the transport extends over a finite range of B forming the characteristic plateaus in R_{xy} and valleys in R_{xx} [15, 19–21]. The description presented here focuses exclusively on the Integer Quantum Hall Effect (IQHE) which is the regime of most importance to the investigations in this thesis. There also exists systems that exhibit quantization when the Landau level filling factor equals rational fraction values, known as the Fractional Quantum Hall Effect (FQHE), as can be observed at $\nu = \frac{5}{3}$ in Fig. 1–4 [20–22].

1.1.4 Resistively Detected Nuclear Magnetic Resonance

Since its discovery by Bloch [23] and Purcell [24] in the 1940s, nuclear magnetic resonance (NMR) has grown to become a powerful scientific tool with many applications including spectroscopy and medical imaging. In essence, nuclear magnetic resonance is a technique used to observe the transition of nuclei between two spin states. Fig. 1–6 shows an example of a typical NMR experiment, where a sample is placed into a uniform d.c. magnetic field. A coil attached to a radio-frequency oscillator is also wrapped around the sample providing a relatively weak second magnetic field $\mathbf{B_1}$ oriented perpendicular to $\mathbf{B}$.

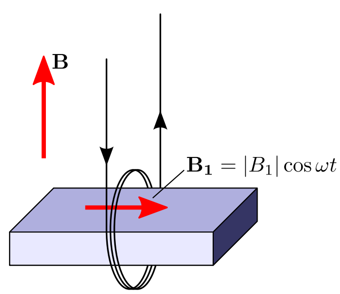

Figure 1–6: Illustration of a typical NMR experiment where the sample is placed in a uniform external magnetic field $\mathbf{B}$ and the in-plane magnetic field (perpendicular to $\mathbf{B}$) created by the coil is $\mathbf{B_1}$.

When the sample is exposed to an external magnetic field, the nuclear magnetic moments $\boldsymbol{\mu}$ of the nuclei will precess at the Larmor precessional frequency

$$\nu_L = \gamma_n B, \tag{1.11}$$

where γ_n is the gyromagnetic ratio of the nuclei and B is the magnetic field.

The potential of a nuclear magnetic dipole in an external magnetic field is $E = -\boldsymbol{\mu} \cdot \mathbf{B}$, which is at its minimum when projection of the magnetic dipole is *aligned* with $\mathbf{B}$ and maximum when oriented *opposite* to $\mathbf{B}$. Fig. 1–7(b) demonstrates an example energy level diagram for a spin $\frac{1}{2}$ system.

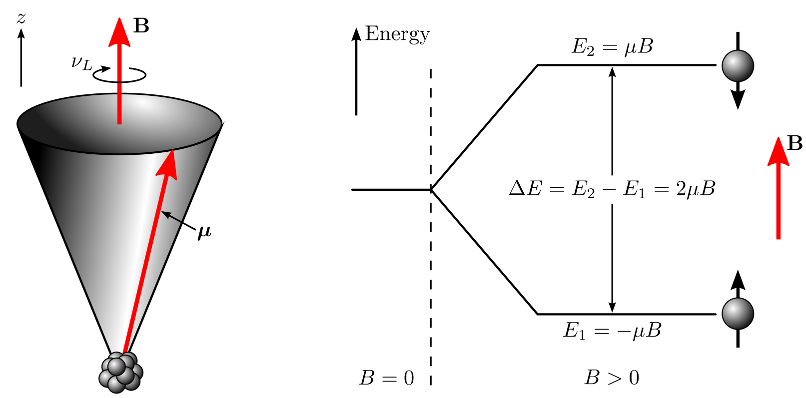

(a) (b)

FIGURE 1–7: (a) When placed in an external magnetic field, the magnetic moment of the nuclei will precess with frequency ν_L. (b) Energy level diagram for spin $\frac{1}{2}$ nucleus. When the spin is aligned with the magnetic field, it resides in its lowest energy state E_1 and in the higher energy state E_2 when the spin is oriented opposite to the field.

When the frequency of the oscillator driving the coil reaches the Larmor frequency, a torque will be generated on the precessing magnetic moments causing them to transition between two spin states. The spin state transitions cause energy to be absorbed by the system which can be detected inductively by an antenna.

Since it probes the bulk of the sample, the major limitation of classical NMR is when the number of nuclei becomes too small for detection. Using modern techniques, the minimum number of spins required for detection is approximately 10^{16}. For systems with smaller scales such as quantum dots (10^6–10^{10} spins), carbon nanotubes

($< 10^3$ spins per tube) and GaAs/AlGaAs 2DEGs ($< 10^{15}$ spins for a 30 nm well), the number of spins is too low to be detected using traditional NMR methods.

A number of techniques have been developed to increase the detection resolution in systems with small number of spins, including optically pumped NMR (OP-NMR) [25, 26], magnetic resonance force microscopy [27], and resistively detected NMR (RDNMR) [28]. RDNMR, which was first discovered by von Klitzing's group in 1988, has become a powerful tool in studying quantum Hall systems by utilizing the coupling between the electrons and nuclei that is a result of the strong hyperfine interaction, $\mathcal{A}\mathbf{I} \cdot \mathbf{S}$, in a GaAs/AlGaAs heterostructure [29, 30].

In an external magnetic field $\mathbf{B} = B_z$, the total electronic Zeeman energy can be written as

$$E_z = g^* \mu_B B S_z + \mathcal{A} \langle I_z \rangle S_z \tag{1.12}$$

where g^* is the effective electronic g factor, S_z is the electron spin parallel to the magnetic field, $\mathcal{A}$ is the hyperfine coupling constant, and $\langle I_z \rangle$ is the nuclear spin polarization. The Zeeman energy in Eq. 1.12 can be rewritten as

$$E_z = g^* \mu_B (B + B_N) S_z \tag{1.13}$$

where the finite nuclear polarization creates an effective magnetic field known as the *Overhauser shift* $B_N = \mathcal{A} \langle I_z \rangle / g^* \mu_B$. In quantum Hall systems, the magnetoresistance in the thermally activated region near the zero resistance states,

$$R_{xx} \propto e^{-\Delta/2k_B T}, \tag{1.14}$$

is a function of the energy gap Δ which, in turn, is dependent on the Zeeman energy. This relation demonstrates that R_{xx} is in fact sensitive to changes is nuclear spin since its value is determined to some extent by the hyperfine coupling.

In GaAs, the induced effective magnetic field B_N will be in opposition to the external magnetic field since the effective g factor is negative ($g^* = -0.44$), which will lower the total Zeeman energy in Eq. 1.13. Depolarizing the nuclear spins in the sample by applying transverse radio frequency (RF) radiation at the isotope's NMR resonance will increase the Zeeman gap as $B_N \to 0$. In quantum Hall systems at odd Landau level filling factors (i.e. $\nu = 1$) the gap energy Δ varies directly with the Zeeman gap. Therefore, a change in the nuclear polarization will result in a measurable change in R_{xx} providing the detection mechanism for the nuclear magnetic resonance [31, 32].

1.1.5 Light-Matter Interactions and Optical Pumping

In semiconductors, there are a number of possible pathways for photon interaction to occur. Photons can interact with the crystal lattice and convert their energy into heat by interacting with impurity atoms or with defects in the semiconductor crystal. The most important interaction is that between a photon and valence band electron, as depicted in Fig. 1–8, where the photon has energy $E = h\nu = \frac{hc}{\lambda}$ and the semiconductor's bandgap energy is $E_g = E_c - E_v$.

If the photon has energy $E = h\nu < E_g$ it will be unable to elevate the valence electrons to the conduction band. The semiconductor will be transparent to photons in this energy range and they will not be absorbed. If $h\nu > E_g$, the photon has enough energy to interact with a valence band electron and provides enough energy to elevate it into the conduction band leaving a hole in the valence band. This process is known as electron-hole pair generation.

After the electron is elevated to a higher energy level, the system will eventually return to thermal-equilibrium and the electron will recombine with the hole in the conduction band to release the excess energy through numerous pathways including,

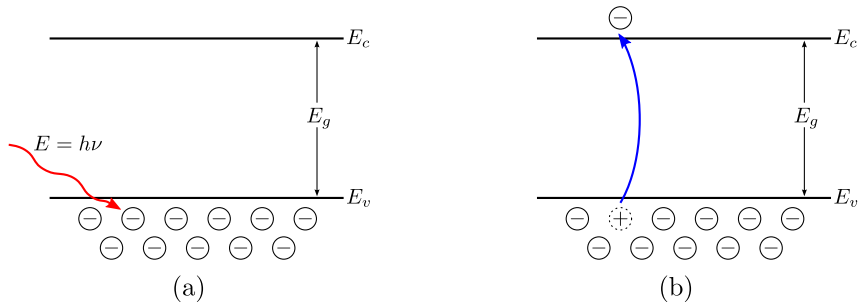

FIGURE 1–8: (a) A photon with energy $E = h\nu > E_g$ is absorbed by a conduction band electron. (b) The electron is elevated into the valence band, creating an electron-hole pair.

but not limited to, photon emission, lattice vibrations (phonons) and the generation of Auger electrons.

1.1.6 Double Resonance & Dynamic Nuclear Polarization

The discovery of double resonance, where one excites a single resonant transition in a system while simultaneously monitoring a second transition, has been one of the most important developments of magnetic resonance. The reasons for utilizing double resonance are vast and plentiful including polarizing nuclei, enhancing sensitivity, simplifying complex spectra and generating coherent radiation (lasers and masers).

The *Pound-Overhauser double resonance* method makes use of spin-lattice relaxation mechanisms and involves a family of energy levels whose populations are ordinarily held in thermal equilibrium by thermal relaxation processes. Saturating one of the energy level transitions binds them together, forcing the two populations to be equal. The thermal relaxation processes will then redistribute the populations of all the remaining levels. This redistribution can produce unusual population differences that may lead to interesting properties, such as the upper of two energy levels having a *larger* population than the lower, or a small population difference may be enhanced to become much larger [33].

This effect was first theorized by Overhauser [34] who predicted that, if one saturated the conduction electron spin resonance in a metal, the nuclear spins would be polarized 1000 times more strongly than their normal polarization in the absence of electron saturation. The first double resonance experiment was conducted by Pound on the ^{23}Na nuclear resonance of $NaNO_3$ where a $\frac{5}{3}$ factor enhancement of the $+\frac{1}{2}$ to $-\frac{1}{2}$ transition was seen after he saturated the $\frac{3}{2}$ to $\frac{1}{2}$ transition [35]. The second double resonance experiment was conducted by Carver who was the first to demonstrate dynamic nuclear polarization and to validate Overhauser's revolutionary prediction [5].

A Model System

As an example, one can look at the energy levels of a simple system with nuclear spin $I = \frac{1}{2}$ that is coupled to an electron of spin $S = \frac{1}{2}$, and acted on by an external magnetic field B_0. The system can be described by the Hamiltonian

$$\mathcal{H} = \gamma_e \hbar B_0 S_z + \mathcal{A}\mathbf{I}\cdot\mathbf{S} - \gamma_n \hbar B_0 I_z \tag{1.15}$$

where the subscripts e and n denote electrons and nuclei. This model assumes in the strong field approximation that $\gamma_e \hbar B_0 \gg \mathcal{A}$. The result is that S_z nearly commutes with $\mathcal{H}$ so its eigenvalue m_S can be considered a good quantum number. Since now only $\mathcal{A} I_z S_z$ has diagonal terms, the effective Hamiltonian is

$$\mathcal{H} = \gamma_e \hbar B_0 S_z + \mathcal{A} I_z S_z - \gamma_n \hbar B_0 I_z \tag{1.16}$$

If we take the quantum number of I_z (m_I) as another good quantum number, the energy eigenvalues of the system will be

$$E = \gamma_e \hbar B_0 m_S + \mathcal{A} m_I m_S - \gamma_n \hbar B_0 m_I \tag{1.17}$$

where $m_S = \pm\frac{1}{2}$ and $m_I = \pm\frac{1}{2}$. For an applied alternating field, the selection rules for induced transitions will be $\Delta m_S = \pm 1$, $\Delta m_I = 0$ for electron spin resonance, and $\Delta m_S = 0$, $\Delta m_I = \pm 1$ for nuclear resonance. The system will have four allowed resonance transitions, shown in Fig. 1–9, with resonance frequencies

$$\omega_e = \gamma_e B_0 + \frac{\mathcal{A}}{\hbar} m_I \tag{1.18a}$$

$$\omega_n = \gamma_n B_0 - \frac{\mathcal{A}}{\hbar} m_S. \tag{1.18b}$$

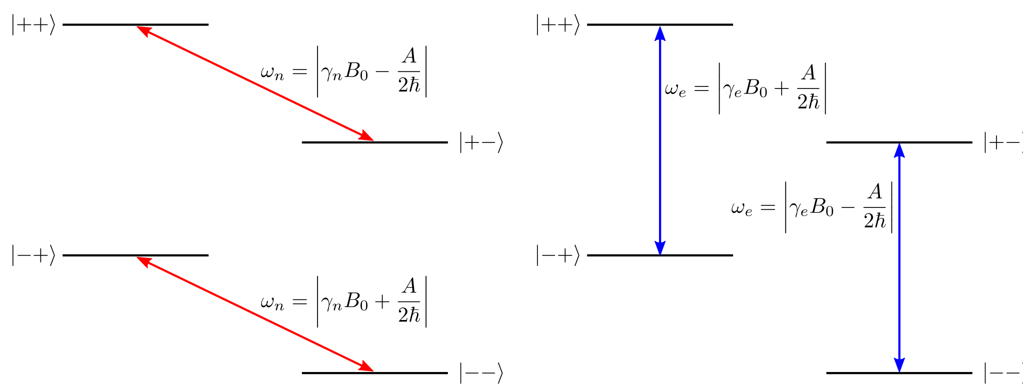

(a) Nuclear resonance transitions (b) Electron resonance transitions

FIGURE 1–9: Energy level diagram for the allowed transitions of a simple system with $S = \frac{1}{2}$ and $I = \frac{1}{2}$ in an applied magnetic field B_0. Each state is denoted in a simplified form where, for example, $|+-\rangle$ represents $m_S = +\frac{1}{2}$, $m_I = -\frac{1}{2}$. γ_n is assumed to be negative in this figure [33].

If we assume a less simplistic view of the electron spin-nuclear spin coupling and include the effects of dipolar coupling, the resulting Hamiltonian will be

$$\mathcal{H} = \gamma_e \hbar B_0 S_z + \mathcal{A}_{x'x'} S_{x'} I_{x'} + \mathcal{A}_{y'y'} S_{y'} I_{y'} + \mathcal{A}_{z'z'} S_{z'} I_{z'} - \gamma_n \hbar B_0 I_n \tag{1.19}$$

where x', y' and z' are a set of principal axes [33].

The solution to the general Hamiltonian in Eq. 1.19 leads to an energy level diagram that is similar to Fig. 1–9 as long as $\gamma_e \hbar B_0 \gg |\mathcal{A}_{x'x'}|$, $|\mathcal{A}_{y'y'}|$ and $|\mathcal{A}_{z'z'}|$. If these assumptions are true, then m_S is still a good quantum number, but m_I may not be. In this case, the lowest order wave functions ψ_i will no longer be

$$\psi_i = |m_S m_I\rangle \, , \tag{1.20}$$

but rather a linear combination of such states

$$\psi_i = \sum_{m_S, m_I} c_{im_S m_I} \, |m_S m_I\rangle \, . \tag{1.21}$$

The result of using the more general Hamiltonian in Eq. 1.19 over that in Eq. 1.15 is that through the application of an alternating field, resonance transitions other than those shown in Fig. 1–9 become possible. These additional transitions are known by convention as *forbidden transitions* [8, 9, 33, 36].

The Overhauser Effect

Although Overhauser's original prediction was focused on the polarization of nuclei in a metal, one can use the simplified model presented in the previous section to illustrate the process he proposed. This example assumes that the principal relaxation mechanisms are electron spin relaxations ($W_{12}, W_{21}, W_{34}, W_{43}$) and a combined nuclear-electron spin flip (W_{23}, W_{32}) as demonstrated in Fig. 1–10.

An alternating field is applied to induce transitions between the ψ_1 and ψ_2 states at a rate W_e, where W_e corresponds to an electron spin resonance. In this case, we will define p_i as the probability of occupying the state ψ_i. A series of differential equations results, (full details provided by Slichter [33]), and the steady state solution results

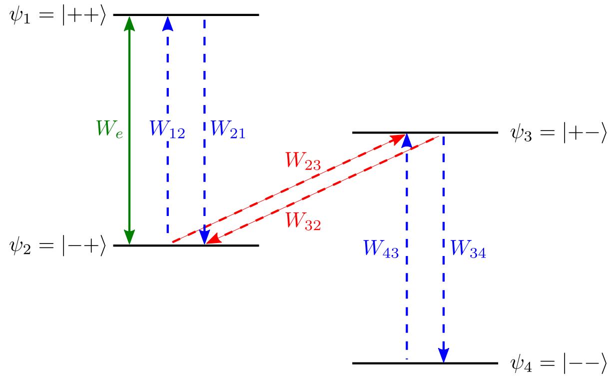

FIGURE 1–10: Energy band diagram for the Overhauser effect. W_{ij} represent the thermally induced transitions that try to maintain thermal equilibrium. Electron spin transitions are shown in blue and combined nucleus-electron spin flips are shown in red. An applied alternating field induces spin transitions at a rate W_e shown in green [33].

are found to be

$$p_1 = p_2 \tag{1.22}$$

$$p_3 = p_4 \frac{W_{43}}{W_{34}} \tag{1.23}$$

$$p_3 = p_2 \frac{W_{23}}{W_{32}} \tag{1.24}$$

where Eq. 1.22 is the due to the clamped populations, and Eq. 1.23 and Eq. 1.24 are the normal thermal equilibrium population ratios for the pairs of states (ψ_3, ψ_4) and (ψ_2, ψ_3) respectively.

Since the pairs (p_3, p_4) and (p_2, p_3) are in thermal equilibrium, the ratio of p_4 to p_2 must also be in thermal equilibrium. For a pair of levels in thermal equilibrium, they can be defined by the Boltzmann ratio B_{ij} where

$$\begin{aligned} p_j &= p_i e^{(E_i - E_j)/k_B T} \\ &\equiv p_i B_{ij} \end{aligned} \tag{1.25}$$

This leads us to rewrite the probabilities as

$$p_1 = p_2 = \frac{1}{2 + B_{23} + B_{24}} \tag{1.26}$$

$$p_3 = \frac{B_{23}}{2 + B_{23} + B_{24}} \tag{1.27}$$

$$p_4 = \frac{B_{24}}{2 + B_{23} + B_{24}}, \tag{1.28}$$

which gives an average nuclear spin polarization of

$$\begin{aligned} \langle I_z \rangle &= \sum_i p_i \langle i | I_z | i \rangle \\ &= \frac{1}{2}\left(p_1 + p_2 - p_3 - p_4\right) \\ &= \frac{1}{2}\frac{2 - B_{23} - B_{24}}{2 + B_{23} + B_{24}}. \end{aligned} \tag{1.29}$$

To look at the significance of this expression, one can look at the high temperature limit where $B_{ij} \cong 1 + \frac{E_i - E_j}{k_B T}$, which results in

$$\begin{aligned} \langle I_z \rangle &= \frac{1}{2}\frac{\gamma_e \hbar B_0 + \left(\frac{\mathcal{A}}{2}\right) + 2\gamma_n \hbar B_0}{4 k_B T} \\ &\cong \frac{1}{2}\frac{\gamma_e \hbar B_0}{4 k_B T} \end{aligned} \tag{1.30}$$

If the sample was not being saturated by an external field, the expectation value of the nuclear spin in thermal equilibrium would be

$$\langle I_z \rangle_{\text{therm}} = \frac{1}{2}\frac{\gamma_n \hbar B_0}{2 k_B T}. \tag{1.31}$$

Comparing Eq. 1.30 and Eq. 1.31, we find that by saturating the electron spin resonance W_e the mean nuclear spin has increased by

$$\frac{\langle I_z \rangle}{\langle I_z \rangle_{\text{therm}}} = \frac{\gamma_e}{2\gamma_n}. \tag{1.32}$$

In the case of a metal, as originally proposed by Overhauser, each electron couples to a number of nuclei so there is only a single electron resonance. This would be equivalent to saturating both electron resonances in our model, so the resulting mean nuclear spin polarization is

$$\frac{\langle I_z \rangle}{\langle I_z \rangle_{\text{therm}}} = \frac{\gamma_e}{\gamma_n}. \tag{1.33}$$

as originally predicted by Overhauser [8, 9, 33, 36].

Polarization by Forbidden Transitions

It was Abragam [37] and Jeffries [38] who independently recognized that these forbidden transitions were not *strictly* forbidden, and in some circumstances they could be used to a great advantage in achieving nuclear polarization. The two possible forbidden transitions for our model system are illustrated in Fig. 1–11.

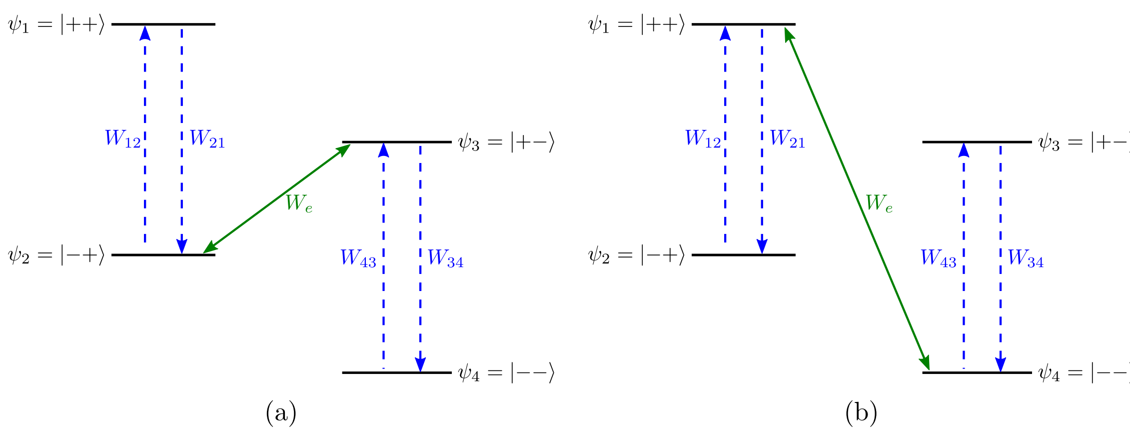

FIGURE 1–11: Energy level diagrams describing the use of forbidden transitions which flip both the electron and nucleus simultaneously to produce nuclear polarization. The transitions W_{en} illustrated in (a) and (b) will produce nuclear polarization of opposite signs. In this model it is assumed that transitions involving and electron spin-flip are the only significant thermal processes [33].

The transitions in Fig. 1–11 can be induced by alternating fields perpendicular to B_0 when the general Hamiltonian in Eq. 1.19 is solved to adequate precision. Although the transition probability W_{en} is often small, it can produce effective population equalization if W_{en} is made larger than the thermal transition rate at which a nucleus flips. To further illustrate this point, we will analyze the saturation of the forbidden transition illustrated in Fig. 1–11(b).

Assuming that the only possible thermal transitions are those shown in the figure, we can immediately see that

$$p_1 = p_4 \tag{1.34a}$$

$$p_2 = p_1 e^{(E_1 - E_2)/k_B T} = p_1 B_{12} \tag{1.34b}$$

$$p_3 = p_4 e^{(E_4 - E_3)/k_B T} = p_4 B_{43} \tag{1.34c}$$

and can therefore see that

$$p_1 = p_4 = \frac{1}{2 + B_{12} + B_{43}} \tag{1.35a}$$

$$p_2 = \frac{B_{12}}{2 + B_{12} + B_{43}} \tag{1.35b}$$

$$p_3 = \frac{B_{43}}{2 + B_{12} + B_{43}}. \tag{1.35c}$$

The average expectation value of nuclear spin I_z is given by

$$\begin{aligned} \langle I_z \rangle &= \sum_i p_i \langle i | I_z | i \rangle \\ &= \frac{1}{2} (p_1 + p_2 - p_3 - p_4) \\ &= \frac{1}{2} \frac{B_{12} - B_{34}}{2 + B_{12} + B_{43}} \end{aligned} \tag{1.36}$$

To look at the significance of this expression, we once again can look at the mean nuclear spin polarization in the high temperature limit

$$\langle I_z \rangle = \frac{1}{2}\frac{\gamma_e \hbar B_0}{2k_B T}. \tag{1.37}$$

This leads to an enhancement over the normal polarization of

$$\frac{\langle I_z \rangle}{\langle I_z \rangle_{\text{therm}}} = \frac{\gamma_e}{\gamma_n} \tag{1.38}$$

which is once again the result originally predicted by Overhauser [8, 9, 33, 34, 36].

Dynamic Nuclear Polarization through Optical Methods

The first example of this dynamic nuclear polarization (DNP) by photoelectrons was observed in ^{29}Si by Lampel who found that, under excitation in circularly polarized light, the NMR signal was much larger than what was observed without optical pumping [39]. The mechanism of the strong influence of the excitation light polarization on the nuclear spins has been well studied [40]. The effect of polarization at nuclear resonance is due to the change of the hyperfine magnetic field B_N (see Eq. 1.13) experienced by the photoelectrons as a result of the dynamically polarized nuclei. A comprehensive review of this effect is presented by Paget and Burkovitz [9].

In order to determine the dependence of the nuclear spin polarization on the handedness of the polarized light, one must first look at the interactions of the photons and the electron spin system. The degree of circular polarization $\mathcal{P}$ of the luminescence light can be defined as

$$\mathcal{P} = \frac{L_+ - L_-}{L_+ + L_-}, \tag{1.39}$$

where $L_{\pm}$ is the intensity of the $\sigma^{\pm}$-polarized component of the total luminescence [9, 41]. Here we define σ^{+} and σ^{-} respectively as right and left handed circularly polarized light.

Under optical pumping conditions, the same selection rules describe the absorption of a circularly polarized photon and the radiative recombination of a spin-polarized electron. As a result, we find that the mean electronic spin is related to the degree of circular polarization by

$$\langle S \rangle = -\mathcal{P}. \tag{1.40}$$

In these systems the interaction between a single electron of spin $\mathbf{S}$ and a nucleus of spin $\mathbf{I}$ is described by the Fermi contact Hamiltonian $\mathcal{H}_F$ [8]. Since this Hamiltonian is of the form $\mathcal{A}\mathbf{I}\cdot\mathbf{S} = \mathcal{A}\left[\frac{1}{2}\left(I_+S_- + I_-S_+\right) + I_zS_z\right]$, the nuclei are dynamically polarized allowing for the simultaneous reversal of a nuclear spin and an electronic spin. The value of the mean nuclear spin is then

$$\langle I \rangle = \frac{I\left(I+1\right)}{S\left(S+1\right)}\left[\langle S \rangle - \langle S_T \rangle\right], \tag{1.41}$$

where I and S are the nuclear and electronic spins respectively, $\langle S \rangle$ is the optical pumping mean electronic spin and $\langle S_T \rangle$ is the electronic mean spin in the external magnetic field. This equation holds true for $\langle I \rangle \ll 1$ and, in most cases, the thermodynamic mean $\langle S_T \rangle$ is negligible compared to $\langle S \rangle$ and $\langle I \rangle$ is simply proportional to $\langle S \rangle$ [9]. Therefore, we find the resulting relationship between luminescence polarization and nuclear spin polarization to be

$$\langle I \rangle \propto -\mathcal{P}. \tag{1.42}$$

It has also been shown that only localized electrons (see Fig. 1–5) are efficient at dynamically polarizing nuclear spins [9]. These localized electrons are found in all practical cases, and can be trapped on shallow donors [42] or in the spatial fluctuations within the conduction band minima of doped semiconductors [41]. This is significant for these studies, as experiments were conducted on the flank of $\nu = 1$ in the region of the localized states.

A Qualitative Illustration

This complex relationship can be clarified in a simple illustrative argument using conservation of spin angular momentum and the model described in the previous section. Here an attempt will be made to qualitatively describe the interaction of the circularly polarized photons with the system. Although presented for a two level system, this model should also hold true for systems with spins $I > \frac{1}{2}$ and $S > \frac{1}{2}$.

First, it should be noted that the spin angular momentum of a circularly polarized photon is $-\hbar$ for σ^+ and $+\hbar$ for σ^-. One of the finer points of detail is that we cannot define a spin for linearly polarized light but rather, since all the photons are identical, each will have an equal probability of being in an $-\hbar$ or $+\hbar$ state. Therefore, there will be no overall angular momentum imparted by a linearly polarized beam of light. In the case of elliptically polarized light, there is an unequal probability of each being in either spin state so a net angular moment will be imparted to the target [43].

In Fig. 1–12, an example four state system is used, but in this case the system is under excitation by circularly polarized photons. In Fig. 1–12(a) a σ^+ photon interacts with the $m_S = +\frac{1}{2}$ due to conservation of spin angular momentum, and the photoexcited electron's spin flips to become $m_S = -\frac{1}{2}$. This will create an excess of electrons in states $\psi_2 = |-+\rangle$ and $\psi_4 = |--\rangle$. This population increase in ψ_2

and ψ_4 will cause a redistribution of the other state's populations. Specifically, the excess electrons in ψ_2 can relax through the hyperfine pathway W_{23} and repopulate ψ_3. This will result is an overall $\langle I_z \rangle > 0$. We note that rather than a full saturation of the transition as described previously for the Overhauser effect, it is suggested that a steady state population inversion will result from the photoexcitation.

For the opposite case in Fig. 1–12(b), one sees that the σ^- photons interact with the $m_S = -\frac{1}{2}$ increasing the populations of ψ_1 and ψ_3 through conservation of spin momentum. Here the hyperfine relaxation pathway W_{32} will restore some of the population to ψ_2. The populations in (ψ_3, ψ_4) will be greater than (ψ_1, ψ_2), producing in an overall $\langle I_z \rangle < 0$.

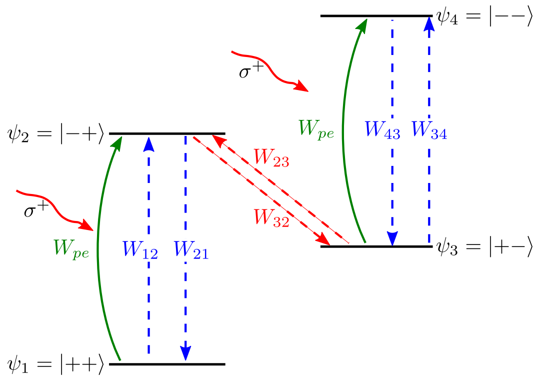

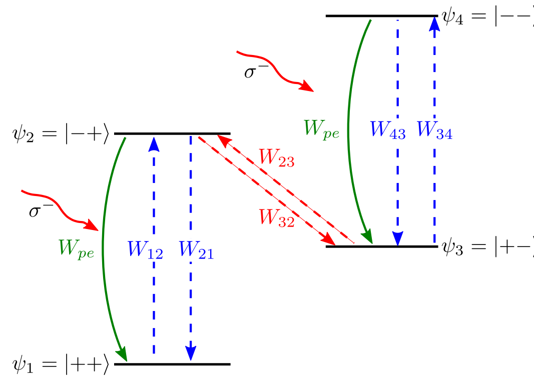

FIGURE 1–12: Illustration of the optical Overhauser effect in a simple four state system under photoexcitation by (a) right handed and (b) left handed circularly polarized light.

Although Paget's mechanism presented here for the dynamic nuclear polarization in GaAs has been well studied in the literature, it should be noted that contradictory results have been found. In the work by Barrett, results following this relationship as found in Eq. 1.42 were not observed. It was noted that this may have been the result of the the high magnetic fields in their experiments affecting the selection rules, equilibrium polarization of electrons and holes, or the relaxation processes which can affect the resulting nuclear polarization [25]. This observation hints that, under certain conditions, the dynamic nuclear polarization process may not be as straightforward as previously thought.

1.2 Thesis Objectives & Organization

The main objectives of this thesis is to experimentally investigate the effect of illuminating a GaAs/AlGaAs quantum well in the integer quantum Hall regime with different polarizations of near infrared laser light. Each chapter of this thesis will focus on a different set of experiments performed on the system.

Chapter 2 will present the design and implementation of the polarization controller system used to illuminate the sample during the transport measurements. A numerical model will be presented along with supporting experimental data. In addition, the complications that arise when the controller is used in a system containing a superconducting magnet are explored.

In Chapter 3 the results of magneto-optical transport measurements performed using the polarization controller and a single GaAs/AlGaAs quantum well sample are discussed. The dependence of the $\nu = 1$ quantum Hall state on the polarization of the light used for excitation was investigated using resistively detected NMR techniques. In addition, dynamics experiments were conducted to determine the relaxation rate of the system under different polarizations of light.

Chapter 4 presents an examination of different phenomena found to occur in a quantum Hall system under photoexcitation by low power infrared laser light. A thorough investigation of these phenomena's dependence on contact geometry, temperature and laser power is presented.

CHAPTER 2

Polarization Controller

THE ABILITY TO ACTIVELY CONTROL the polarization of light is a vital necessity to utilize dynamic nuclear polarization to manipulate nuclear spins. In this chapter we introduce the design and operation of a polarization controller for laser-light in the near infrared spectrum with an optical fiber held at low temperatures where all of the optical components are kept outside of the cryogenic system. A complete analysis of the polarization controller is presented in the case where the optical fiber is enclosed inside a large magnet, and it is shown that the scheme can be used to produce well-defined light polarizations even in the presence of a relatively strong magnetic field.

2.1 Controller Operation

The polarization controller presented builds upon the work of Heismann et al. and consists of three birefringent waveplates, two $\lambda/4$ separated by one $\lambda/2$ [44], as depicted in Fig. 2–1. This combination of waveplates is capable of transmitting any arbitrary state of polarization (SOP) into the optical fiber by simply varying the waveplate angles [44]. The polarization axes of the two $\lambda/4$ waveplates in the apparatus are separated by 90° with respect to each other. The angles α and β

represent the amount of clockwise rotation of the slow axis from the vertical for each of the $\lambda/4$ and $\lambda/2$ waveplates respectively. These waveplate angles were initialized with a computer camera to an accuracy of 0.2°. The controller uses a 5 mW near infrared diode laser of wavelength $\lambda \approx 800$ nm along with a single-mode optical fiber (SM800, 125 μm cladding diameter) to transmit the polarized light onto a sample mounted inside of a commercial ^{3}He cryostat (Janis HE-3-SSV) containing a 9 T superconducting magnet. In order to deflect the back-reflected signal of the light entering the fiber, the injector end was cleaved at an angle of $\sim$ 8°. Neglecting losses, it is assumed that the optical fiber acts as a birefringent transformation on the light [45], and as such, the backward propagating light undergoes the inverse polarization change as the light propagating in the forward direction. Therefore, the birefringent fiber and waveplates are known as *reciprocal* media [46]. There exists a natural birefringence of the optical fiber which is primarily due to mechanical deformation such as twisting and stress inside the fiber [47]. These properties may vary with each experiment so each time the cryostat is placed in the Dewar the fiber at room temperature is fixed in place for the remainder of the experiment.

The novelty of the polarization controller presented is based on the isolation and measurement of the small amount of light reflected back from the interface at the end of the fiber. In order to provide information about the light exiting the fiber, the back-reflected signal is isolated using a polarizing cube beam splitter located between the laser source and the first waveplate. The purpose of the cube is twofold, it first acts as a vertical polarizer for the source laser light before it interacts with the retarding waveplates. Secondly, it acts as a horizontal polarization filter and a 45° mirror for the back-reflected light.

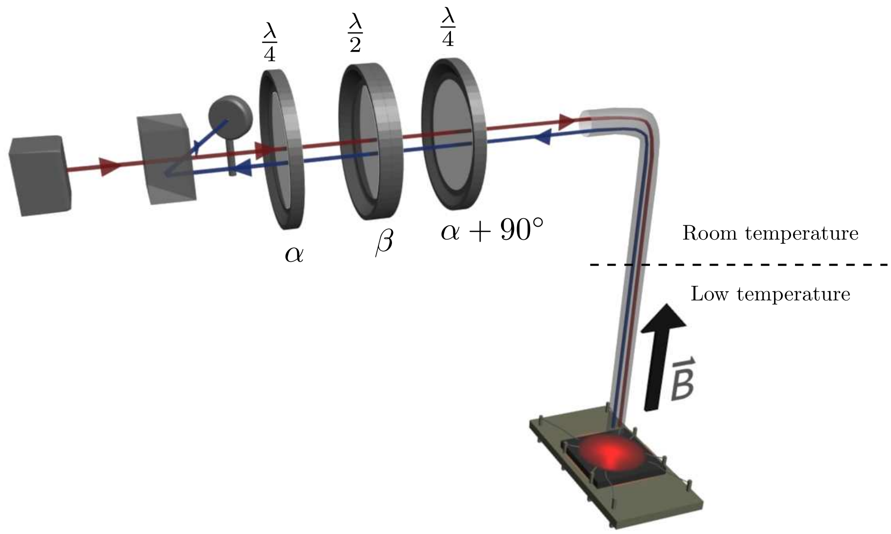

Figure 2–1: Illustration of the polarization controller apparatus. The red path shows the forward propagating light and the blue denotes the path of the back-reflected light. All of the optical components are at room temperature while the light is transmitted onto a sample at $T \approx 270\,\mathrm{mK}$.

The usefulness of the polarization controller is best described by an example as follows. For the case of transmitting right hand circularly polarized light (σ^+) on to the sample, the overall transformation of the light travelling through the three waveplates and the optical fiber will be equivalent to that of a single $\lambda/4$ waveplate at 45°. At the end of the fiber, a small percentage of the light is not transmitted. This back-reflected light undergoes a transformation at the interface due to the transition from a higher to a lower index of refraction. The reflection does not affect linear polarized light but changes the handedness of the circularly polarized light, e.g. σ^+ becomes σ^-. In this case, the back-reflected σ^- light will travel in the reverse direction through the fiber and waveplates and it will experience the inverse transformation (equivalent to a $\lambda/4$ waveplate at $-45°$). This results in a net polarization of horizontally linear light that interacts with the polarizing cube such that a maximum signal is transmitted to the back-reflection detector. A maximum intensity in the back-reflected signal implies transmission of circularly polarized light (σ^+ or σ^-) onto the sample. Although the output is known to be circularly polarized, its *handedness* remains ambiguous. This limitation of the back-reflection technique is a result of using the intensity where all of the phase information is lost.

In the case of transmitting linear polarized light along the vertical axis, no polarization changes occur due to the reflection at the end of the fiber. The back-reflected signal will maintain its original linearly polarized state which will be cancelled out by the horizontal polarizing axis of the beamsplitting cube resulting in a minimum intensity in the back-reflected signal. Therefore a minimum intensity in the back-reflected signal implies transmission of linearly polarized light onto the sample.

The intensity of the back-reflected signal is measured as a function of the waveplate angles α and β, and is used to produce a two dimensional map of the transmitted light's polarization. These $\alpha - \beta$ maps are produced by setting a desired α and sweeping through various β angles in 2° increments with a computer controlled stepper motor, defining the waveplate angles necessary to transmit any arbitrary polarization of light onto the sample mounted inside of the ^{3}He cryostat.

2.2 Simulation Without A Magnetic Field

Using Jones matrix transformations, a simulation can be made of the back-reflected signal intensity detected in the experiment [48]. The $\lambda/4$ and $\lambda/2$ waveplates are represented by the matrices $Q(\alpha)$ and $H(\beta)$ respectively and the optical fiber by the general birefringent transformation matrix $F(\phi, \psi, \theta)$,

$$Q(\alpha) = \frac{1}{\sqrt{2}} \begin{bmatrix} 1 - i\cos 2\alpha & -i\sin 2\alpha \\ -i\sin 2\alpha & 1 + i\cos 2\alpha \end{bmatrix} \tag{2.1}$$

$$H(\beta) = \begin{bmatrix} -i\cos 2\beta & -i\sin 2\beta \\ -i\sin 2\beta & i\cos 2\beta \end{bmatrix} \tag{2.2}$$

$$F(\phi, \psi, \theta) = \begin{bmatrix} e^{i\phi}\cos\theta & -e^{-i\psi}\sin\theta \\ e^{i\psi}\sin\theta & e^{-i\phi}\cos\theta \end{bmatrix} \tag{2.3}$$

where the angles of the waveplates α and β were defined previously and the angles $\{\phi, \psi, \theta\}$ describe the physical birefringent properties of the optical fiber. Here ϕ and θ describe the ellipticity of birefringence and rotation of the birefringence axes and ψ is representative of the phase shift that occurs along the fiber [49].

The first step in the simulation is to calculate the light's state of polarization as it exits the end of the fiber onto the sample. The Jones matrix transformations, shown in Eq. 2.4, starts (reading from right to left) with vertical linear polarized light exiting the polarizing cube $[\ 0 \quad 1\ ]^T$ and then proceeds through the three retarding waveplates (Q, H, Q) and the optical fiber (F).

$$S_{sample} = F(\phi, \psi, \theta)\, Q(\alpha + 90°)\, H(\beta)\, Q(\alpha) \begin{bmatrix} 0 \\ 1 \end{bmatrix} \tag{2.4}$$

The calculation for the back-reflected signal, shown in Eq. 2.5, starts with the light that is reflected at the end of the optical fiber which is described as the complex conjugate of S_{sample},

$$S_{back} = \begin{bmatrix} 1 & 0 \\ 0 & 0 \end{bmatrix} Q(\alpha)^{-1} H(\beta)^{-1} Q(\alpha + 90°)^{-1} F(\phi, \psi, \theta)^{-1} (S_{sample})^{*}. \tag{2.5}$$

The light travelling in the backward direction undergoes the inverse of each transformation it experienced while travelling through the waveplates and fiber in the forward direction. The light then interacts with the polarizing beam splitter cube which acts as a horizontal linear polarization filter and reflects the light onto the detector. The intensity measured by the back-reflection detector is proportional to $I_{detector} \propto |S_{back}|^2$.

Fig. 2–2 shows a comparison between experimental and simulated $\alpha - \beta$ maps. The simulation matches up qualitatively well with the experimental data in both shape and position, albeit with some small variations in measured intensity. This may be due to physical effects not taken into account in the Jones matrix model, such as the sharp temperature gradient of the fiber (room temperature to $\leq 4\,\mathrm{K}$).

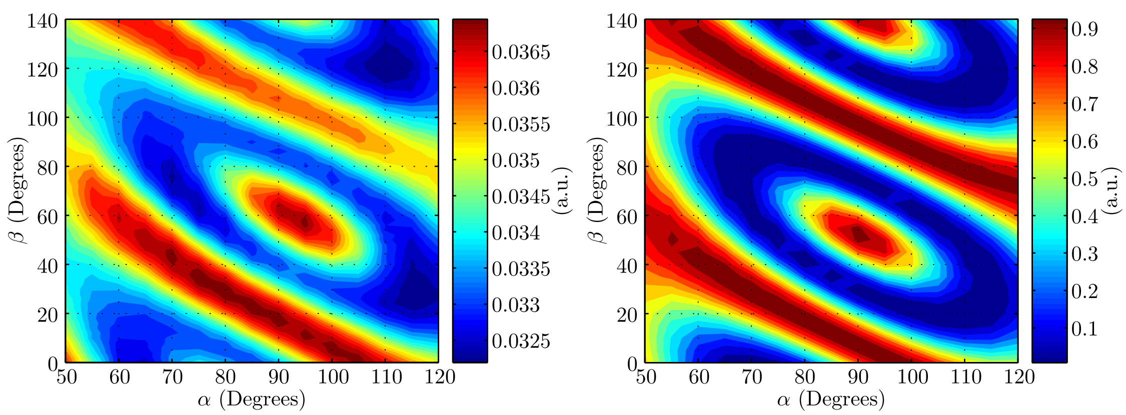

(a) Experiment (b) Simulation

FIGURE 2–2: Contour maps of the back-reflection intensity at zero magnetic field as a function of waveplate angles α and β. (a) Typical experimental data taken at low temperature, $T \approx 270\,\mathrm{mK}$. (b) Jones matrix simulation using Eq. 2.4 and Eq. 2.5 with fitting parameters $\phi = 1.3\pi$, $\psi = 0.64\pi$ and $\theta = 1.26\pi$ for the optical fiber.

2.3 Magnetic Field Effects

When light travelling through a medium of minimal birefringence interacts with a magnetic field $\mathbf{B}$, the linear polarization plane is rotated by an angle Γ. This is known as the Faraday effect [50]. In an ideal fiber, the Faraday rotation angle is given by

$$\Gamma = V \int_L \mathbf{B} \cdot \mathbf{dl} \tag{2.6}$$

where V is the Verdet constant, L is the interaction length, and $\mathbf{B}$ is the magnetic field. The Verdet constant is a physical property of the fiber and is dependent on the wavelength of the propagating light [51] as well as thermal coefficients of the fiber [52]. As a result, there will be an additional rotation to the polarization of the light travelling through the optical fiber as the strength of the magnetic field inside the cryostat is increased.

Adding a further complication to the back-reflection measurement scheme, the media in which Faraday rotations occur are termed *non-reciprocal*: light travelling in the reverse direction does not undergo the inverse of the transformation it experienced while propagating in the forward direction. For example, if light travelling in the $+z$ direction through a length of fiber L in a magnetic field is rotated by an angle $+\Gamma$, a wave travelling in the opposite direction will undergo a rotation of angle $-\Gamma$ about the new direction of propagation ($-z$). The net effect of a round trip through the medium is that the polarization plane will have a total rotation of 2Γ with respect to the original polarization at $z = 0$ [46]. In the experiment presented, the measured back-reflected light will undergo twice the Faraday rotation as the light shining on the sample.

In order to accommodate for this, the Jones matrix simulation model was extended to include a Faraday rotation transformation [53].

$$R(\Gamma) = \begin{bmatrix} e^{i\Gamma} & 0 \\ 0 & e^{-i\Gamma} \end{bmatrix} \tag{2.7}$$

Where Γ was previously defined in Eq. 2.6. In this model, it is assumed that no birefringent transformations occur in the region at the end of the fiber where the Faraday rotation occurs. To minimize these effects in the experiment, the small length of fiber exposed to the magnetic field is fixed in place without any bends to limit physical stresses to the fiber. The light exiting the fiber in a magnetic field can now be approximated by the Jones matrix transformations

$$S_{sample} = R\left(\Gamma\right) F\left(\phi, \psi, \theta\right) Q\left(\alpha + 90°\right) H\left(\beta\right) Q\left(\alpha\right) \begin{bmatrix} 0 \\ 1 \end{bmatrix}. \tag{2.8}$$

The back-reflected signal then undergoes the following transformation,

$$S_{back} = \begin{bmatrix} 1 & 0 \\ 0 & 0 \end{bmatrix} Q\left(\alpha\right)^{-1} H\left(\beta\right)^{-1} Q\left(\alpha + 90°\right)^{-1} F\left(\phi, \psi, \theta\right)^{-1} R\left(\Gamma\right)^{\dagger} \left(S_{sample}\right)^{*} \tag{2.9}$$

where $R\left(\Gamma\right)^{\dagger}$ denotes the Hermitian conjugate of the Faraday rotation matrix.

The field gradient curve, shown in Fig. 2–3, was provided by the manufacturer of the superconducting magnet. It describes the magnetic field strength as a function of position along the z-axis of the cryostat. The provided curve was derived for the maximum field strength of the magnet, 9 T, where $\int_L \mathbf{B} \cdot \mathbf{dl} \approx 1.08\,\mathrm{m\,T}$ was found by numerical integration of the field gradient. The gradient shows a fairly sharp cutoff; therefore the integral in Eq. 2.6 can be reasonably approximated by a uniform magnetic field B over a fixed length l, as shown in Fig. 2–3.

$$\Gamma = V \int\limits_L \mathbf{B}(l) \cdot \mathbf{dl} \approx VBl \tag{2.10}$$

To compare the experimental data with the simulations, the initial fitting parameters $\{\phi, \psi, \theta\}$ were found for the $\alpha - \beta$ map acquired at $B = 0\,\mathrm{T}$. Fixing these parameters, two other $\alpha - \beta$ maps were produced at different magnetic field strengths.

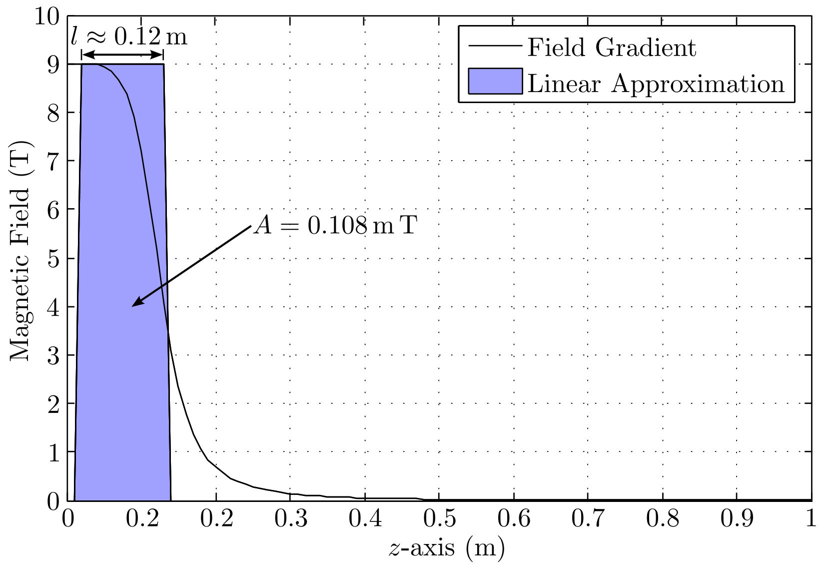

FIGURE 2–3: Magnetic field gradient along the z-axis inside the cryostat where $z = 0$ corresponds to the centre of the superconducting magnet. The shaded region denotes the area of the field where the optical fiber is present starting at $z = 0.019\,\mathrm{m}$. The box shows the approximation of a uniform magnetic field B over a length $l = 0.12\,\mathrm{m}$. The area enclosed by the rectangle is equal to the area under the curve in the field profile.

Using this approximation, the amount of Faraday rotation per Tesla can be used as a fitting parameter for the simulation, where $\Gamma/B = Vl$. A result of this approximation is that changes in V and l are indistinguishable, so the collective term Vl is used. This makes it possible to match the changes in the polarization maps as a function of magnetic field, as illustrated in Fig. 2–4.

The experimental data and simulations match up well in both location and shape at each of the magnetic fields tested for fiber parameters $\{\phi, \psi, \theta\} = \{0.28\pi, 0.2\pi, 1.1\pi\}$ and $Vl = 0.06 \pm 0.005\,\mathrm{rad\,T^{-1}}$. These values were found by fitting the parameters by inspection to match up with the corresponding experimental maps. The error in Vl comes from the qualitative analysis where the values within that range produce reasonable agreement with the experimental data. It should be noted that the experimental data shows a decrease in the peak to peak signal amplitude as the magnetic

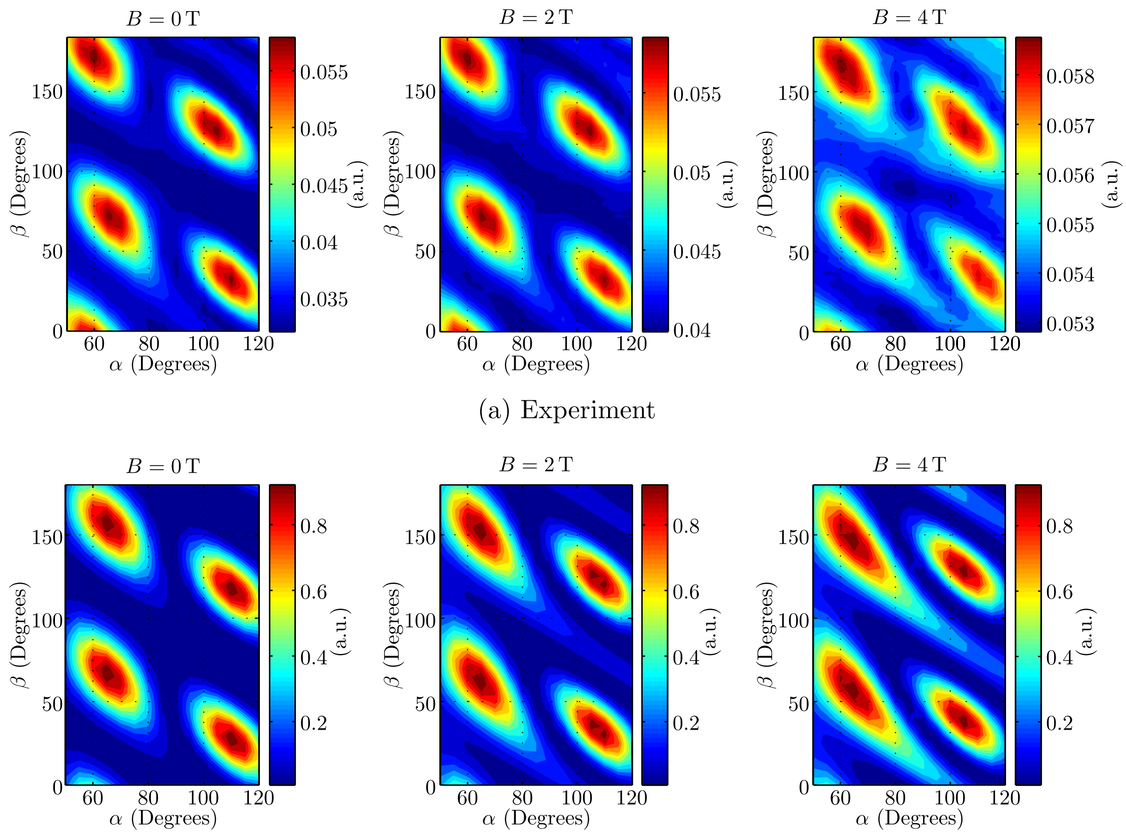

(a) Experiment

(b) Simulation

Figure 2–4: Contour maps showing the polarization controller output in different magnetic fields. (a) Maps of experimental data ($T \approx 270\,\mathrm{mK}$) and (b) the corresponding Jones matrix simulations. As the magnetic field is increased, the regions of circularly polarized light begin to rotate counter-clockwise and become distorted.

field strength is increased. The origin of this behaviour is not well understood at this time, however, it is speculated that the efficiency of the controller may be related to the non-uniformity and non-linearity of the magnetic field along the optical fiber.

A search of the literature was conducted to find comparative results but no results were found in a similar temperature regime. The work by Williams et al. showed that the Verdet constant of SiO_2 optical fibers has a positive linear relationship with temperature in the range of $293 - 423$ K, but no work was conducted at lower temperatures [52]. There was no indication in the literature that using Becquerel's formula to approximate the Verdet constant at the extreme temperatures of the apparatus is valid. As a result, using the same numerical estimation was unfeasible. Although a direct comparison of these results are not possible at this time, the value from the Jones matrix model agrees with the trend that a smaller value of Vl will result at low-temperatures.

2.4 Conclusions

In this chapter the design and operation of our cryogenic polarization controller for near infrared laser light using a back-reflection measurement technique was described. A Jones matrix model was presented to verify the operation of the controller with and without exposure to a strong magnetic field. When operating in a magnetic field, the light travelling through the optical fiber undergoes a Faraday rotation that produces an offset in the polarization measured with the back-reflected signal in comparison to the output at the end of the fiber. This understanding will prove invaluable when using the controller to conduct magneto-optical transport measurements in quantum Hall samples, which will be discussed in Chapter 3.

CHAPTER 3

Magneto-optical Quantum Transport Measurements

THE NUCLEAR SPINS of GaAs have showed great promise as quantum information carriers [4], but the main hindrance to their implementation lies in the ability to control and retrieve the information from their quantum mechanical states. In this chapter an investigation will be conducted on the use of the cryogenic polarization controller presented in Chapter 2 to manipulate the properties of a GaAs/AlGaAs quantum well in the first Landau level of the integer quantum Hall state.

3.1 Experiment

3.1.1 Apparatus

In order to reach the low temperatures required to perform the transport measurements, a commercial ^{3}He refrigerator (Janis HE-3-SSV) was used to work at a base temperature of $T \approx 270\,\mathrm{mK}$. A copper bar was thermally attached to the ^{3}He chamber of the fridge and a sample mount was constructed out of G10 to place the sample in the centre of the magnetic field profile. To thermally link the sample to the fridge, it was placed on top of a copper plate that is directly connected to the copper bar below the ^{3}He pot.

As described in Chapter 2, the light from the polarization controller is directed into the sample through an optical fiber. The fiber is fed into the cryostat using a vacuum feedthrough and sealed using epoxy to preserve the integrity of the vacuum space. The remainder of the fiber was passed down into the chamber of the vacuum can. In order to accommodate any accidental breakages that may occur at the end of the fiber, an extra length of approximately 0.5 m was looped and loosely fixed to the exterior of the charcoal sorb. The loop was maintained with a diameter of approximately 8 cm to prevent any losses that could occur if the fiber was bent past its critical angle. The charcoal sorb's position outside of the magnetic field gradient, as in Fig. 3–1, makes it ideal for mounting the loop. Since it is outside of the B field, no Faraday rotation occurs in this portion of the fiber. The balance of the fiber was then passed through the magnetic shield and held approximately 1 cm above the sample surface. The light emanating from the end of the fiber is unfocused and, as a result, this position above the sample provides a beam spot that covers as much of the surface as possible.

3.1.2 Optics Calibration

In these experiments, the laser used was a 10 mW diode (L808P010) with a wavelength $\lambda \approx 800$ nm. Barrett showed that this was an ideal wavelength for dynamically polarizing GaAs nuclei [25]. Prior to cooling, the optical system was aligned and the output power calibrated to the laser diode driving current. A power meter (Newport model 815) was placed in front of the fiber's output. A small guide, illustrated in Fig. 3–2, was constructed from heavy stock paper and placed over the sensor to maintain the fiber's alignment with the detector and to block out a majority

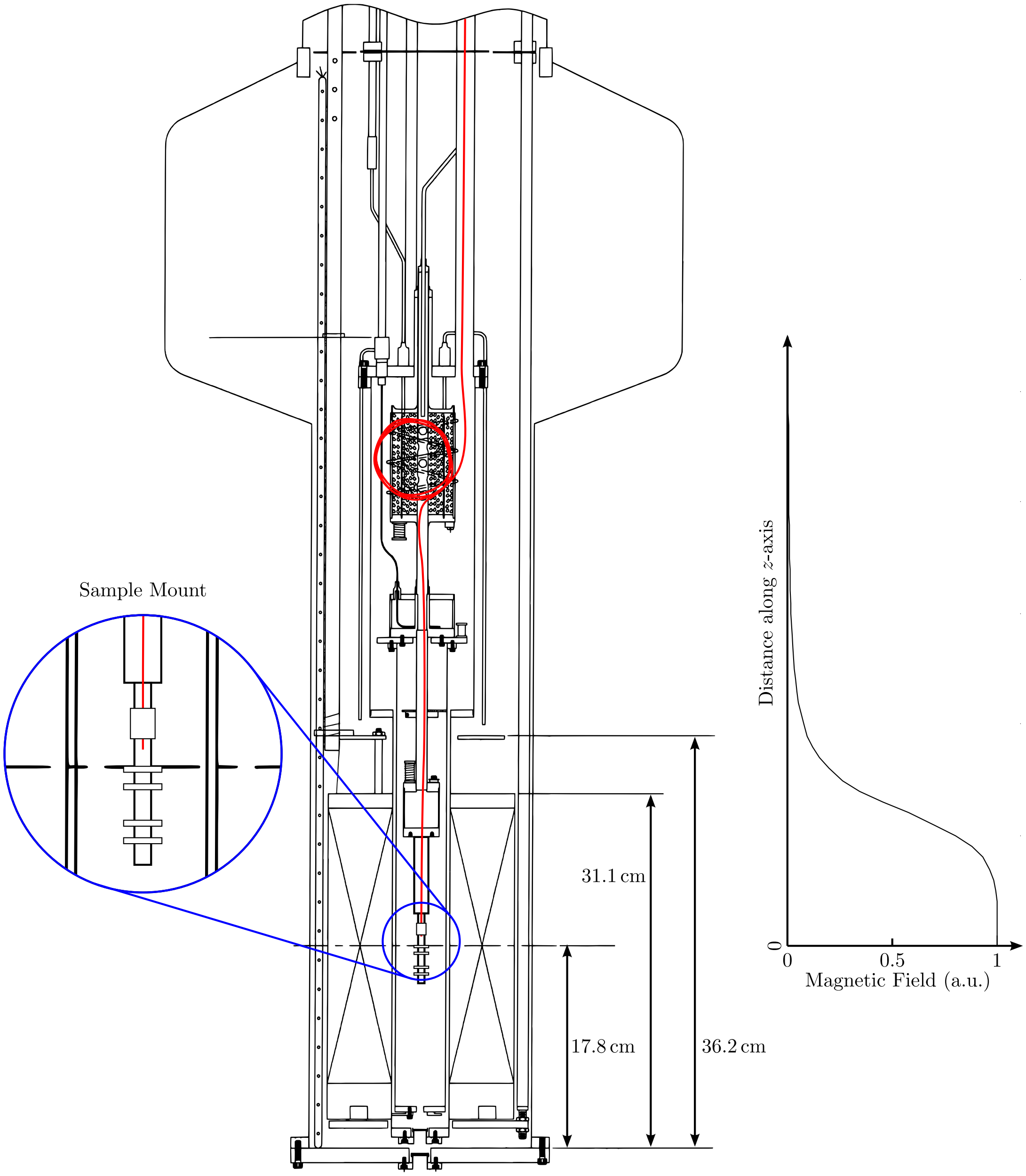

FIGURE 3–1: Illustration of the cryogenic environment in the Janis HE-3-SSV system. The inset on the left demonstrates how the optical fiber (shown in red) is fixed above the sample surface. The vertical magnetic field gradient provided by Janis is shown along the length of the cryostat. This helps demonstrate that the loop of fiber attached to the charcoal sorb is out of the B field.

of the ambient light. Once the output of the fiber was optimized, a calibration curve of the transmitted power was recorded as a function of the laser diode's driving current, shown in Fig. 3–3.

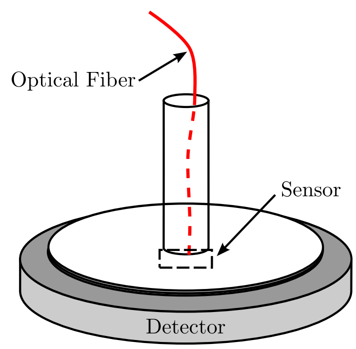

FIGURE 3–2: The configuration used for aligning the optics. The fiber is passed through the guide and aligned with the photosensor inside the power detector.

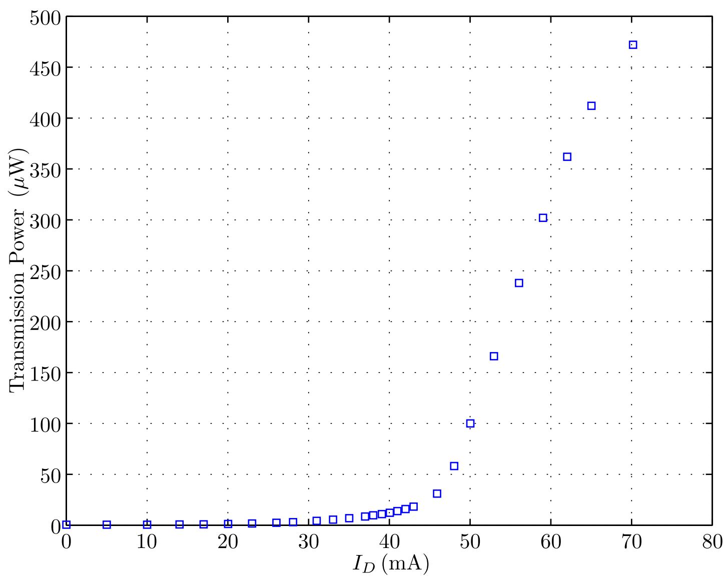

FIGURE 3–3: Example of a typical power calibration curve for the output of the optical fiber with a sharp turn-on current of $I_D \approx 43\,\text{mA}$.

In order to determine if the output power was independent of the polarization, a set of $\alpha - \beta$ maps was produced to compare the intensity of the back-reflection and transmission signals. From the maps in Fig. 3–4, one notes that the power fluctuates by approximately 8% as the waveplates are rotated. However, there does not appear to be a direct correlation between power and polarization.[1]

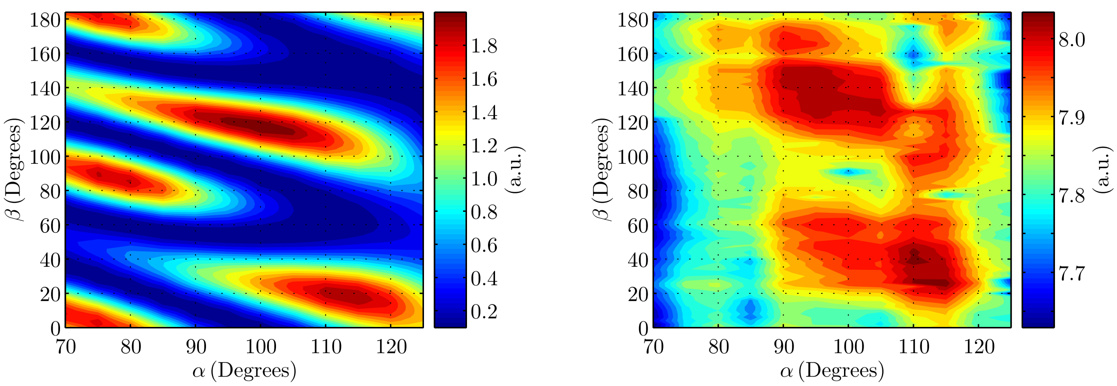

(a) Back-reflection (b) Transmission

FIGURE 3–4: Room temperature $\alpha - \beta$ maps of (a) back-reflection and (b) transmission intensity. In certain map regions, there is a fluctuation in power of approximately 8%.

3.1.3 GaAs/AlGaAs Quantum Well

For the entirety of the experiments presented, a small sample (approximately 5 mm × 5 mm) cut from a GaAs/AlGaAs wafer prepared by our collaborators was used.[2] The wafer was grown using molecular beam epitaxy to form a 30 nm wide well according to the procedure outlined in Fig. A–2 in Appendix A. The full band

---

[1] After this work was completed, more recent measurements have demonstrated that there may in fact be a correlation between polarization and transmission power, although the source of this is unknown at the time of publishing. Further investigation into this relationship is ongoing.

[2] J. L. Reno and M. P. Lilly at Sandia National Laboratories, Center for Integrated Nanotechnologies (CINT), in Albuquerque, NM, USA

structure of the GaAs/AlGaAs quantum well is shown in Fig. 3–5, calculated using the *Poisson 1D* software.[3]

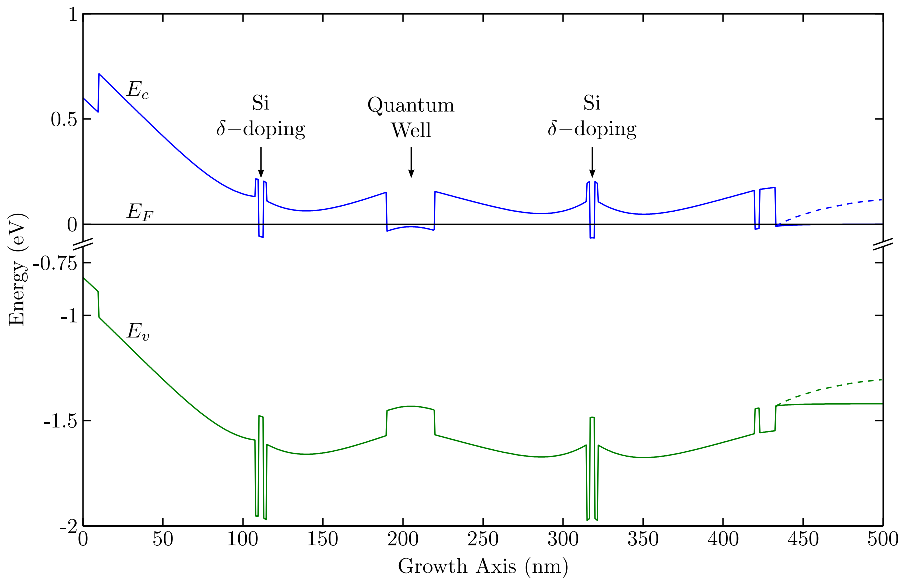

Figure 3–5: Calculation of the approximate band structure of sample according to the growth recipe. Note that the region from 425 nm − 500 nm may not be completely flat. This error is due to improper boundary conditions in the software used to generate the band structure. We believe the structure has some curvature demonstrated as dashed lines in the figure.

One should note that the band structure in Fig. 3–5 is much more complicated than the simple heterojunction example presented in Fig. 1–1. Using a more intricate growth process enables the properties of the quantum well to be tuned for this application. One particular aspect of an advanced growth technique in this wafer is that the silicon δ-dopants are embedded in very narrow additional wells on either side of the main 30 nm well structure. The result is a sample with high mobility

[3] *Poisson 1D* software by G. L. Snider, Department of Electrical Engineering, University of Notre Dame, Notre Dame, IN 46556, USA

($\mu \approx 6 \times 10^6\,\mathrm{cm/V\,s}$) and an approximate electron density $n \approx 3 \times 10^{11}\,\mathrm{cm}^{-2}$ when cooled in the dark.

In order to conduct the quantum transport measurements, indium was used to form ohmic contact with the 2DEG located 200 nm below the sample surface. Small vertical columns of pure indium were placed along the edge of the sample using a finely tipped soldering iron. The sample was placed under vacuum and heated in a 400 °C oven for 25 min, and allowed to cool to room temperature for 2 hr. The diffused indium contacts were connected to a 16-pin header using a wire bonder and indium solder. The layout of the contacts on the sample surface is illustrated in Fig. 3–6(a) and Fig. 3–6(b) gives the standard geometry used for the transport measurements.

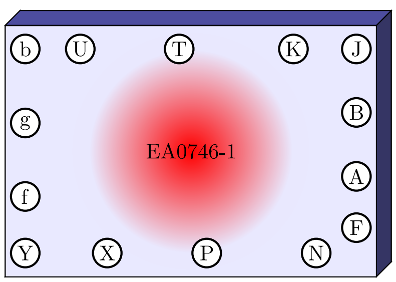

(a)

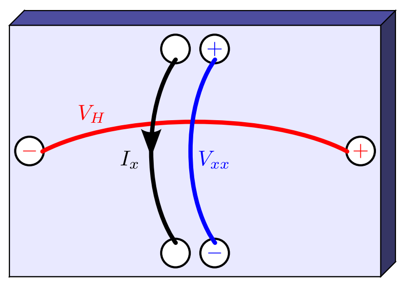

(b)

Figure 3–6: (a) Approximate configuration of the ohmic contacts located on sample. The red gradient represents the beamspot of the unfocused light emanating from the end of the fiber showing its approximate coverage of the sample. (b) Standard measurement geometry for a quantum transport experiments conducted. I_x represents the sourcing current, R_{xx} the magnetoresistance and R_{xy} the Hall resistance.

During the initial cool down, the samples were maintained in a dark state and not exposed to any external sources of energy. Once at liquid helium temperature ($T = 4.2\,\mathrm{K}$), the sample was illuminated with red light from a light emitting diode (LED) to reduce the electron density of the quantum well, as shown in Fig. 3–7(a).

Typically, illuminating a 2DEG sample with photons of near bandgap energy results in an *increase* in the well's electron density. This is generally due to the photoexcitation of the DX centres of the $Al_xGa_{1-x}As$ layer, or through electron-hole generation in the bulk GaAs with a charge separation at the interface. At liquid helium temperatures this positive density change is stable and can only be decreased by significant heating [54]. This is known as Positive Persistent Photoconductivity (PPPC).

In this sample, a permanent *decrease* in the quantum well's electron density was observed after it has been illuminated with red light from a LED. Negative Photoconductivity (NPC) has been reported previously but normally the density was found to increase again after the photoexcitation was removed [54, 55]. Chaves proposed an explanation for NPC and argues that it originates from the optical excitation of electron-hole pairs in the large gap layer and their spatial separation due to the heterojunction's inherent electric field. For quantum well structures with large undoped spacer regions ($L_s \geq 40\,\mathrm{nm}$), such as those found in this sample, the negative photoconductivity can persist for minutes or much longer [56]. This model could account for the Negative Persistent Photoconductivity (NPPC) that was observed in our sample.

It was observed that the density shift remains after a cycle in temperature from $T \approx 0.27\,\mathrm{K} - 4.2\,\mathrm{K}$ but returns to an electron density near that of the dark state after the sample was allowed to warm to $T \approx 40\,\mathrm{K}$, as shown in Fig. 3–7(b).

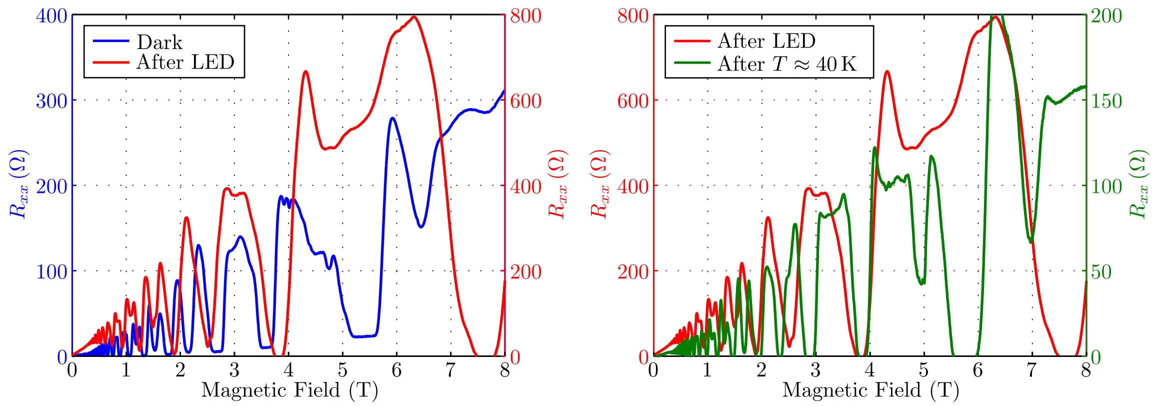

(a) (b)

FIGURE 3–7: (a) Trace of the magnetoresistance as a function of magnetic field before and after the sample was illuminated by the LED. Exposing the sample to 225 μA s ($2 \times 1.5\,\mu$A for 75 s) was usually enough to bring the $\nu = 1$ quantum Hall state within the range of the system's magnet. (b) Density returns to near that of the dark state after the sample is warmed to $T \approx 40$ K. Both traces were taken at base temperature $T \approx 270$ mK.

3.2 Polarization Dependence Sweeps

Once the sample reached an electron density where the valley of $\nu = 1$ was located near $B \approx 6.5\,\mathrm{T} - 7\,\mathrm{T}$, the laser was turned on and the driving current was slowly increased while the sample was grounded. In order to avoid shocking the electrons in the 2DEG, the current was slowly increased until reaching $I_D \approx 42$ mA. This produces a transmission power of approximately 30 μW according to the calibration curve for this specific cooldown, shown in Fig. 3–3.

After the sample was cooled to base temperature, the quality of each of the contacts was determined using the circuit shown in Fig. A–1 of Appendix A. After determining the quality of the contacts, B field sweeps were performed on numerous permutations of I_x^+,I_x^-, V_{xx}^+ and V_{xx}^- to find the configuration that produced the best measurement of the quantum Hall state. For all experiments, a sourcing current $I_x = 100$ nA was used and measurements of V_{xx} and V_{xy} were performed by standard lock-in techniques using either a digital (Stanford SRS-830) or an analog (PAR 124) amplifier.

Once the best contact configuration was ascertained, the magnetic field was moved to the flank of the $\nu = 1$ quantum Hall state, as shown in Fig. 3–8(a). After changing the magnetic field, the sample was left to stabilize for $10 - 15$ minutes to accommodate for any temperature fluctuations that may have occurred due to eddy currents. Normally, a $\alpha - \beta$ map would be produced after any significant change in B due to the considerations discussed in Chapter 2, but in this case the experiment was conducted before the effect of Faraday rotation was completed and therefore no map at the exact measurement field is available. The map of the back-reflection signal in Fig. 3–8(b) was produced at $B = 5.6\,\text{T}$. It is known from Chapter 2 that the Faraday rotation due to 1 T will not significantly change the map and this should be a good representation of the map at $B = 6.77\,\text{T}$.

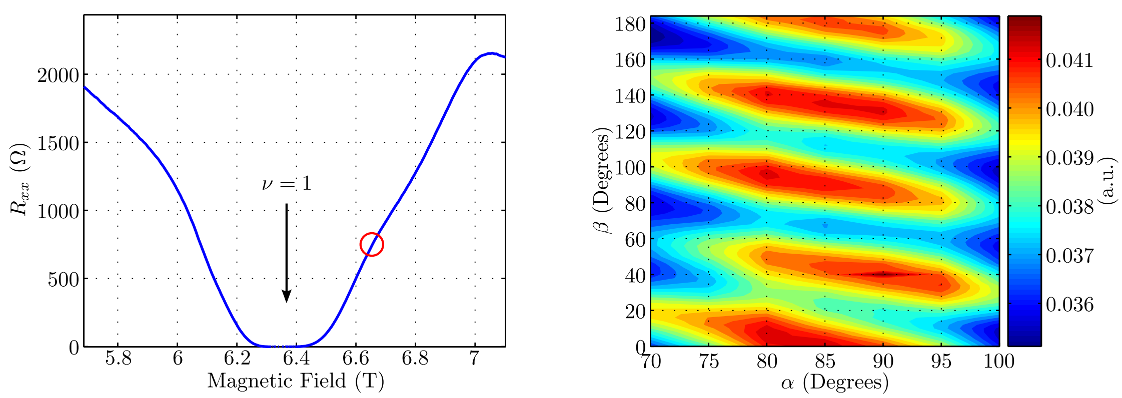

(a) (b)

Figure 3–8: (a) $\nu = 1$ quantum Hall state of the 2DEG. The red circle highlights the approximate location of the optical transport measurements. (b) A contour map of back-reflection intensity measuring the output polarization at $B = 5.6\,\text{T}$.

Ideally, a slice along the vertical of the $\alpha - \beta$ map would be chosen such that the output would cycle through regions of circular (σ^+ and σ^-) and linearly ($||$)

polarized light. For each measurement point, the $\lambda/2$ waveplate was rotated by 2° and the data was acquired for 500 s at each point approximately equal to or longer than the expected nuclear spin relaxation time T_1 [30]. The overall results, shown in Fig. 3–9, demonstrate a clear relationship between changes in magnetoresistance and the polarization of light illuminating the sample. We see that the peaks in back-reflection (denoting σ transmission) correlate well with the peak changes in $\Delta R_{xx}/R_{xx}$, up to ±40%.

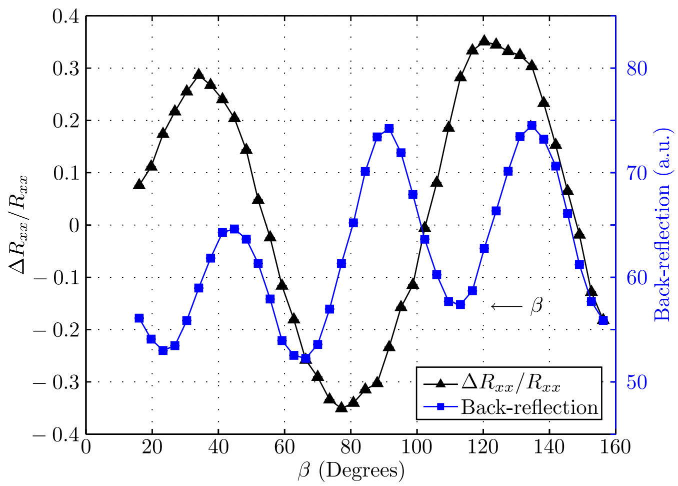

FIGURE 3–9: Changes in magnetoresistance versus light polarization of a GaAs/AlGaAs 2DEG at $T \approx 270\,\mathrm{mK}$, $B = 6.77\,\mathrm{T}$ and the base $R_{xx} = 450\,\Omega$. A small phase offset is found in the back-reflection signal with respect to the resistance oscillations, which is attributed to the additional Faraday rotation that the back-reflected light undergoes in comparison to the light illuminating the sample, as discussed in Chapter 2 [57].

In Chapter 2 we stated the major limitation of this back-reflection technique as its inability to determine the handedness of the transmitted circularly polarized light. Although the *absolute* handedness of the transmitted light is ambiguous, previous work by Mack et al. has demonstrated that adjacent areas of σ light on the $\alpha - \beta$ maps are of opposite handedness [58], labelled hereafter as σ and σ'. In Fig. 3–9, we see that adjacent peaks in back-reflection correspond to changes of R_{xx} in opposite directions.

3.3 2D Maps of Resistance and Polarization

The observations presented in the previous section demonstrate that a clear relationship exists between R_{xx} and the polarization of the light incident on the 2DEG. In an attempt to make these results more robust, similar experiments were repeated through a number of slices along the $\alpha{-}\beta$ map to produce a two-dimensional picture of the relationship between resistance and polarization.

For these experiments, the same procedure outlined in Section 3.2 was used. The B field was set on the right flank of $\nu = 1$ with a base resistance of $R_{xx} \approx 360\,\Omega$. For measurements along the vertical cuts of the $\alpha - \beta$ map, the $\lambda/4$ waveplates were set to a fixed value and the $\lambda/2$ waveplate was rotated in 2° steps. The angles of the $\lambda/4$ waveplates were then rotated by 5° and the measurements were repeated along a new β slice. In Fig. 3–10 we see the results as two dimensional maps of the back-reflection signal and corresponding changes in magnetoresistance.

The correlation between illuminating the sample with circularly polarization and changes in R_{xx} are even more apparent in the 2D maps. The regions of circularly polarized transmission on the back-reflection map correspond directly with changes in $\Delta R_{xx}/R_{xx}$. The regions labelled σ both have the same handedness and correspond a *positive* change in resistance. Conversely, the regions labelled σ' correspond to a *negative* change in resistance.

If one looks closer at the Zeeman energy model given by Eq. 1.13, one can see that a change in the mean nuclear spin polarization $\langle I \rangle$ can be detected using the magnetoresistance R_{xx}. If one follows Paget's result in Eq. 1.42 where $\langle I \rangle \propto -\mathcal{P}$, it

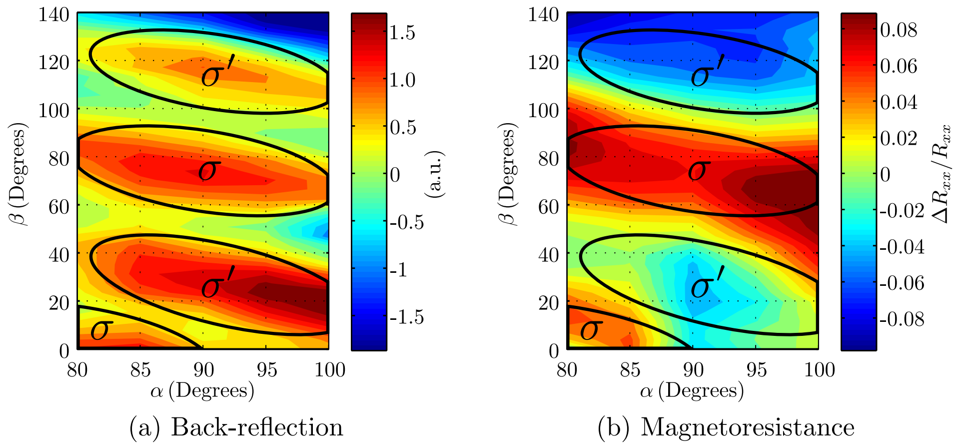

FIGURE 3–10: Two $\alpha - \beta$ maps of (a) back-reflection and (b) $\Delta R_{xx}/R_{xx}$. The regions labelled σ and σ' represent transmission of a different handedness of circularly polarized light. $T \approx 270\,\mathrm{mK}$, $B = 6.770\,\mathrm{T}$, $P \approx 72\,\mu\mathrm{W}$ power output from the fiber .

can be seen that pumping the sample with σ^+ should result in $\langle I \rangle < 0$ and pumping with σ^- should result in $\langle I \rangle > 0$.

Looking closer at the Zeeman energy $E_z = g^* \mu_B (B + B_N) S_z$, where $B_N = \mathcal{A} \langle I_z \rangle / g^* \mu_B$, one can see that a change in $\langle I \rangle$ will affect the magnitude and sign of the Overhauser shift B_N. If $\langle I \rangle > 0$, the Zeeman energy will decrease because B_N will be in opposition to B. If $\langle I \rangle < 0$, the result is an increase in the Zeeman energy gap because B and B_N are in the same direction. In the thermally activated region of $\nu = 1$, this change in the Zeeman gap energy Δ should be detectable as a change in magnetoresistance where $R_{xx} \propto e^{-\Delta/2k_BT}$ (see Eq. 1.14). Therefore, the changes in R_{xx} that are seen as a result of different polarizations may be indicative of polarized nuclei.

3.4 Dynamics Experiments

In the previous two sections, it has been demonstrated that a link exists between the polarization of light used to illuminate the GaAs/AlGaAs 2DEG and the magnetoresistance R_{xx} of the $\nu = 1$ Landau level of the quantum Hall system. The following section describes a series of dynamics experiments that were conducted to probe the origins of this relationship.

To perform these measurements, the system was set up in a similar fashion to the optical sweeps described previously. A $\alpha - \beta$ map of the back-reflection signal was produced after the B field was set on the flank of $\nu = 1$. Using the map in Fig. 3–11(a) as a guide, a vertical slice of β was found that traverses through regions of both σ and $||$ output. The waveplates were then set to a σ region and allowed to stabilize for a minimum of 500 s. While recording the magnetoresistance, the $\lambda/2$ waveplate was quickly rotated (< 1 s) using the computer controlled stepper motor to change the output to a region of linear polarization. In Fig. 3–11(b), the results of the first such dynamics measurement are seen. The fiber's output polarization was changed to a linear state at $t = 0$ s resulting in a behaviour that clearly follows an exponential decay, with an overall $\Delta R_{xx} \approx -95\,\Omega$ and a decay time constant of $\tau_1 = 340 \pm 10$ s.

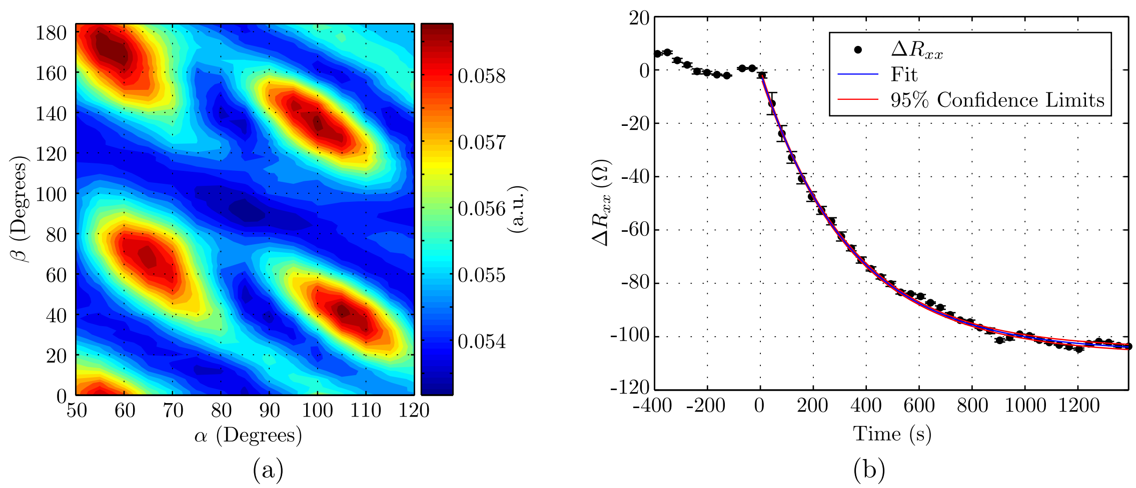

FIGURE 3–11: (a) $\alpha - \beta$ map of back-reflection at $B = 7.1561$ T. (b) A measurement of the magnetoresistance decay as the polarization of light illuminated on the sample was changed from σ to $||$ at $t = 0$ s.

In subsequent measurements, the same process was repeated but the polarization was changed in the opposite direction. In this case, the sample was stabilized under $||$ illumination and then the output was quickly changed to σ. Fig. 3–12 depicts an example result from these experiments. The change in polarization from $|| \rightarrow \sigma$ in Fig. 3–12(a) results in a magnetoresistance change of $\Delta R_{xx} \approx +75\,\Omega$ and an exponential behaviour with a time constant of $\tau_1' = 360 \pm 20\,\mathrm{s}$. After the sample had stabilized, the process was reversed and measurements were taken of the transition from $\sigma \rightarrow ||$, shown in Fig. 3–12(b). Again, one sees an exponential decay with a time constant of $\tau_1 = 440 \pm 20\,\mathrm{s}$ and an overall $\Delta R_{xx} \approx -80\,\Omega$. In general, the process appears to be very reversible and the equilibrium magnetoresistance under each pumping condition remains the same.

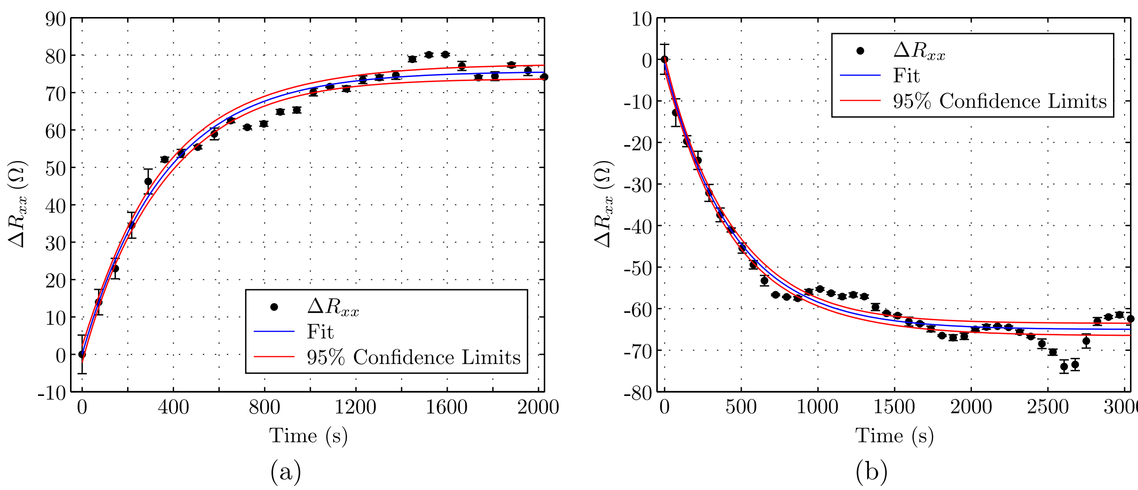

FIGURE 3–12: Decay of magnetoresistance near $\nu = 1$ as the polarization of light shining on the sample is changed at $t = 0\,\mathrm{s}$ from (a) $|| \rightarrow \sigma$ and (b) $\sigma \rightarrow ||$.

It should be noted that in the previous experiments, all of the measurements were performed using σ regions having the same handedness of circularly polarized light. An additional measurement was taken using a circularly polarized region of the opposite handedness labelled as σ' in Fig. 3–11(a). Fig. 3–13 shows the results from a measurement of the transition of output polarization from $\sigma' \rightarrow ||$. Although the change in resistance is not as well behaved as the previous examples, one should recognize that, as expected, this transition ($\sigma' \rightarrow ||$) results in a *positive* change in R_{xx} whereas the previous transitions ($\sigma \rightarrow ||$) all result in a *negative* change in R_{xx} [9]. The relatively small change in resistance, compared to $\Delta R_{xx} \approx \pm 90\,\Omega$ found above, may possibly be due to an offset due to Faraday rotation. If the transmitted polarization output was significantly offset from the measured back-reflection $\alpha - \beta$ map, the waveplate position may not be on the peak of the local maximum. This could significantly reduce the efficiency of the optical pumping mechanism.

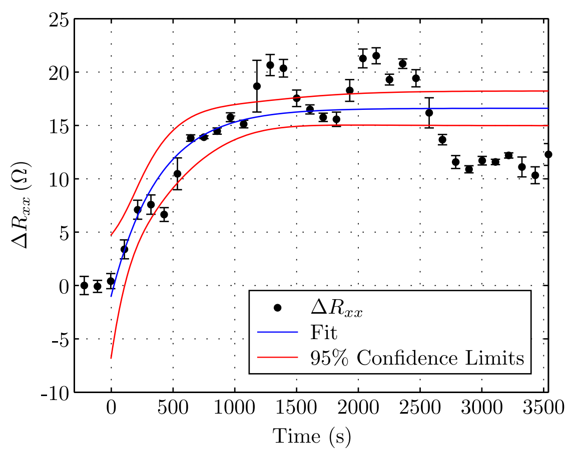

FIGURE 3–13: Decay curve of magnetoresistance with a time constant of $\tau_1 = 380 \pm 110\,\mathrm{s}$ as the polarization is changed from $\sigma' \rightarrow ||$ at $t = 0\,\mathrm{s}$.

3.5 Conclusions

This chapter has presented the results of magneto-optical transport measurements performed to examine the interconnection between the magnetoresistance near the $\nu = 1$ quantum Hall state of a GaAs/AlGaAs 2DEG and the polarization of light shining on the sample surface. Measurements in both 1D and 2D were found to demonstrate a clear connection between the handedness of the circularly polarized light shining on the sample and the resulting change in R_{xx} of up to 40%. This result is significant because although nuclear polarizations of only 1% are required to detect a change in resistance [30], it has been reported that nuclear polarizations as high as 40% have been achieved with optical pumping in GaAs samples [59].

Dynamics experiments were also used to further probe the origins of this relationship. An exponential behaviour was found for the decay from a circularly pumped state to an unpumped state under illumination of linearly polarized light. The time constants τ_1 for these decays were all in the range of $300\,\mathrm{s} - 400\,\mathrm{s}$ which is consistent with the order expected for the decay time constant T_1 of polarized nuclear spins in GaAs on the flank of $\nu = 1$ [30]. These experiments also demonstrated that the transitions from different handedness of σ to $||$ result in *opposite* changes in magnetoresistance, consistent with the magneto-optical transport measurements. The results presented reinforce the hypothesis that the nuclear spins of the GaAs are being polarized through dynamic nuclear polarization under illumination of near infrared laser light. Although the evidence is supportive, future experiments will need to be performed using traditional NMR methods to provide conclusive proof that the relationship found is truly a result of the nuclear spin polarization in GaAs.

CHAPTER 4

Laser Induced Phenomena in GaAs/AlGaAs Quatum Wells

During the course of the investigations presented in this thesis, an interesting behaviour was observed in the quantum Hall traces of GaAs/AlGaAs quantum wells exposed to low power near infrared laser light ($\lambda \approx 800\,\mathrm{nm}$). Under illumination, a series of unexplained features were found in the R_{xx} valleys, including but not limited to, $\nu = 1$. This chapter presents the preliminary results of an investigation to uncover the origin of these phenomena.

4.1 Zero Resistance States Under Laser Illumination

While conducting a series of transport measurements to determine the best set of contacts for a quantum Hall trace, an unexplained series of zero resistance states was discovered in a magnetic field trace of R_{xx}. This startling observation is an immediate reminder of the microwave induced zero resistance states found in GaAs/AlGaAs 2DEGs by Mani et al. [60]. Although similar in nature, these experiments were performed in a much different energy regime that in the system presented here.

The measurements were repeated recording both R_{xx} and R_{xy} to determine the Landau level filling factor ν of all the zero resistance states in the trace, shown in Fig. 4–1. It is noted that the features present in R_{xx} show a strong hysteretic behaviour with the B field sweep direction. Upon close inspection, it is noted that the slope of the Hall resistance is not uniform and actually increases at higher magnetic fields ($B > 4\,\mathrm{T}$). Perhaps the most startling result of Fig. 4–1 is that a number of these zero resistance states *do not* coincide with plateaus in R_{xy} as one would expect in a quantum Hall system (integer or fractional). The R_{xy} plateaus that *do* coincide with a zero resistance state are offset from the centre of the valley. These observations may suggest an inhomogeneity in the quantum well and that the geometry of the sample contacts may play an important role in the understanding of these features.

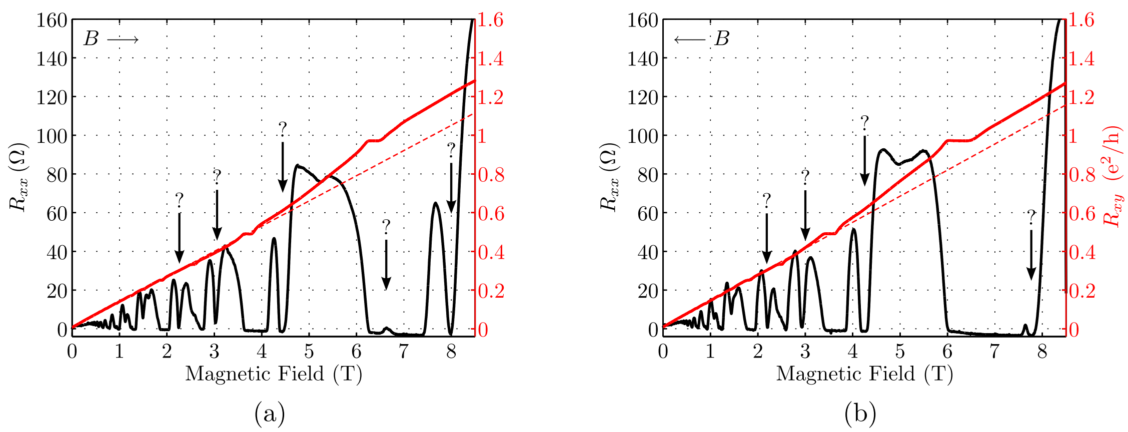

Figure 4–1: Transport sweeps of R_{xx} and R_{xy} with B (a) increasing and (b) decreasing. The dashed red line is a linear fit to the Hall resistance for $B < 2\,\mathrm{T}$ and extrapolated to show the change in curvature of R_{xy} at higher magnetic fields.

4.2 Contact Dependence

In order to examine the effects of geometry, the same transport measurements were repeated using different contact configurations, as shown in Fig. 4–2. The contact maps in the inset of each figure show that each configuration probes a different region of the electron gas. In Fig. 4–2(a) and Fig. 4–2(b), the contacts used for the source current were switched from the centre of the sample to the left edge, resulting in a significant difference in slope of the Hall resistance between the two configurations. Overall, this would suggest that the electron density in the centre of the 2DEG is much lower than the density of the left side.

Some of these results are similar to those found by Shields who studied below bandgap laser excitation in a GaAs/AlGaAs quantum well [61]. While illuminating different regions of the sample, the Hall resistance was measured to determine the electron density of the 2DEG and it was found that the local electron density was reduced in the locality of the laser spot. A significant change in density was observed with both focused and unfocused light. Although the same curvature in R_{xy} that was found in Fig. 4–2 was not seen, only data in the range $B = 0\,\mathrm{T} - 4\,\mathrm{T}$ is available. This however is still in the linear range of the data in this experiment.

Shields proposed that for excitation light with energy *below* the bandgap, the reduction of the quantum well's electron density was due to photoexcitation of the thick GaAs buffer layer. Under illumination, the photoexcited electrons in the buffer would be swept to the front of the sample and collect at the GaAs/AlGaAs interface at the top of the buffer layer, whereas the holes would be swept towards the growth initiation surface.

This process continues until a sufficient amount of charge builds up at the opposite ends of the buffer layer to reduce the electric field across the buffer layer, thereby creating an equilibrium that is dependent on the intensity of illumination. The resulting photovoltage will act like a depleting back gate bias on the quantum well by raising the potential of the GaAs/$\mathrm{Al}_x\mathrm{Ga}_{1-x}\mathrm{As}$ interface at the top of the

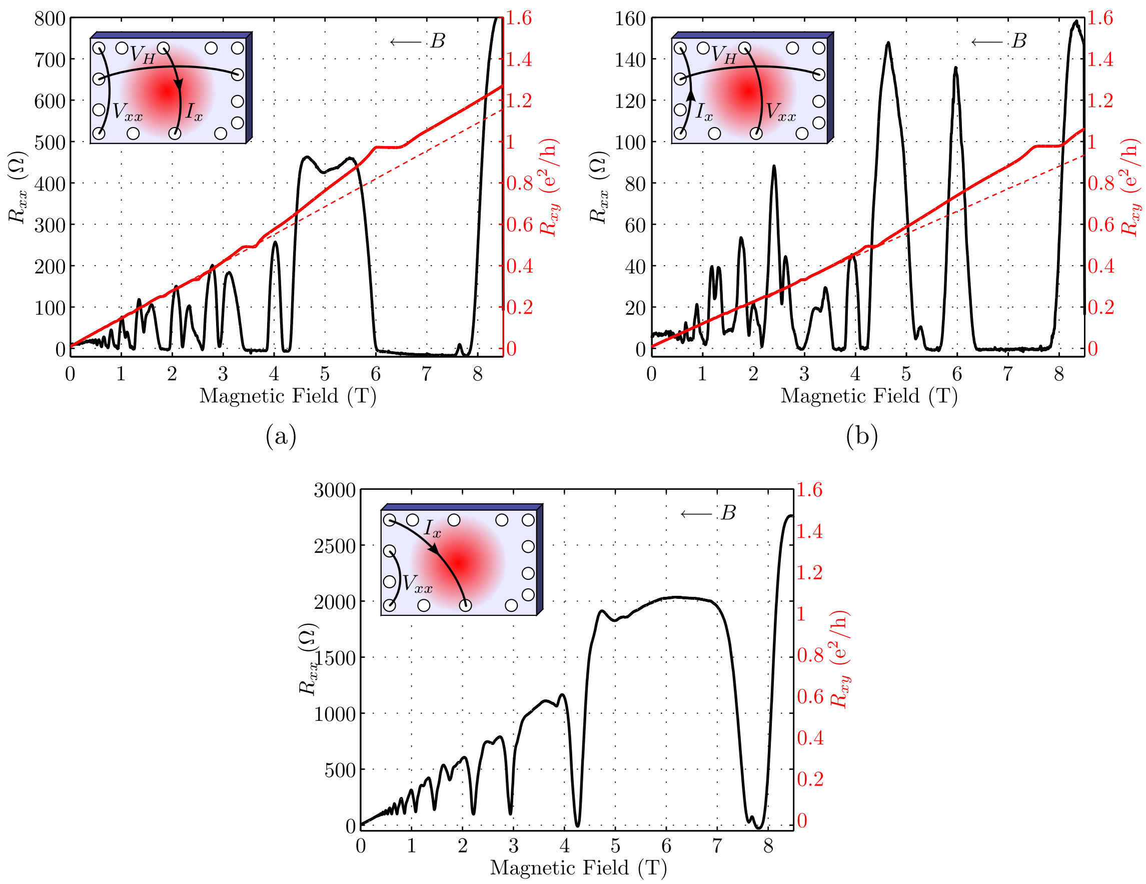

Figure 4–2: Comparison of transport measurements taken using different contact configurations on the GaAs/AlGaAs sample. The only difference between (a) and (b) is that the source current is moved from the centre of the sample to the left side. In (c) the left side of the sample is probed showing only a single density.

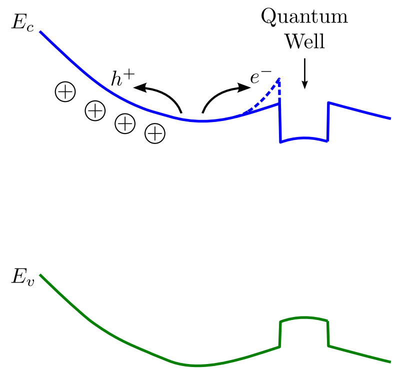

Figure 4–3: Illustration of the band structure modifications that result from photoexcitation with energy below that of the bandgap. In the illuminated region, the build up of charge raises the potential at the GaAs/AlGaAs interface which acts like a depleting back gate bias and reduces the local electron density in the 2DEG [61].

buffer layer. The electrons will flow away from illuminated regions within the plane of quantum well, reducing the local density [61].

In terms of magnetoresistance, the critical factor appears to be the geometry of the four terminal measurement. In Fig. 4–2(a) and Fig. 4–2(b), the contacts for I_x and V_{xx} are not physically close to each other and the additional zero resistance minimas are observed. In Fig. 4–2(c), where the contacts are located closer together, there appears to be only one clear density present and the trace is more representative of a traditional quantum Hall sample. These observations appear to point to an inhomogeneity in the quantum well as a result of laser illumination.

4.3 Temperature Dependence

In order to further understand the origins of these zero resistance states, it is important to understand the energy scales in which they occur. To accomplish this, a full series of temperature dependence measurements of the quantum Hall states were performed up to $T \approx 2.3\,\mathrm{K}$. For each data set, the sample temperature was fixed using a Lakeshore 340 temperature controller and allowed to reach equilibrium and stabilize for 30 min before sweeping the magnetic field. In each case, the magnetic field was swept up and down from $B = 0\,\mathrm{T} - 8.5\,\mathrm{T}$ at a rate of $dB/dt = 0.09376\,\mathrm{T\,min}^{-1}$. The sample was allowed to restabilize before sweeping in the opposite direction to reduce any heating effects from eddy currents. All measurements were were conducted at a constant laser driving current $I_D = 40.05\,\mathrm{mA}$ which corresponds to an power of $P \approx 12\,\mu\mathrm{W}$ illuminating the sample. For the remainder of the experiments, the contact configuration shown in Fig. 4–2(a) was used. The results of the temperature dependence are shown in Fig. 4–4.

The most apparent feature in Fig. 4–4(a) and Fig. 4–4(b) is that the electron density of the 2DEG has a very strong dependence on temperature. This is demonstrated by the gradual shift right of the R_{xx} valleys as the temperature is increased. In order to further demonstrate the temperature dependence of the electron density, the mean density of each sweep was calculated using the location of each Hall plateau centres even though the slope of R_{xy} changes with B. The temperature dependence in Fig. 4–5 indicates that there is a saturation of the electron density in the low and high temperature ranges.

A simple Boltzmann model can be used extract an energy scale from this temperature dependence data. The optical excitation of the laser will create a steady state density of holes in the valence band and electrons in the conduction band (excitons) which are in addition to the electrons present in the well prior to illumination. Assuming that the system is near thermal equilibrium, it is expected that the ratio of free electrons to excitons will be that of a Boltzmann factor. Using this model, a

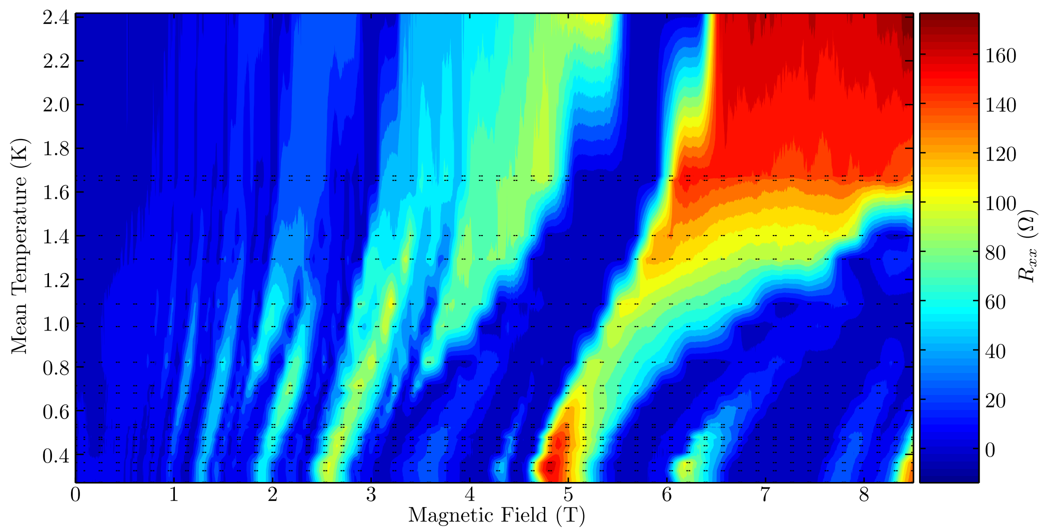

(a) B increasing

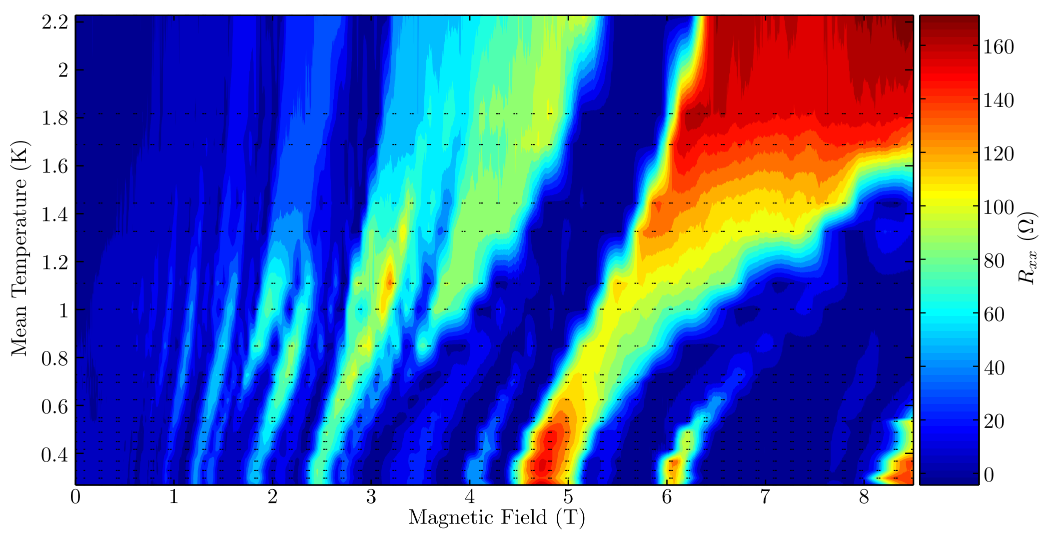

(b) B decreasing

FIGURE 4–4: Magnetic field sweeps (a) up (b) down showing the temperature dependence of a GaAs/AlGaAs quantum well under constant illumination from near infrared laser light. A clear change in the electron density of the quantum well is evident by the shift of the R_{xx} valleys as the temperature increases. The step-like nature in the plots is due to the interpolation method used to generate the contour.

crude prediction for the expected density is of the form

$$n = n_0 + n_L \left(\frac{e^{\frac{-E_b}{k_B T}}}{1 + e^{\frac{-E_b}{k_B T}}} \right), \tag{4.1}$$

where n_0 is the electron density prior to illumination, n_L is the optically generated total electron density (free electrons and electrons bound to excitons) and E_b is the binding energy of an exciton. The model in Eq. 4.1 has been applied to the data in Fig. 4–5 and demonstrates good qualitative agreement to the behaviour of the electron density over this range of temperatures. Using n_L and E_b as fitting parameters, we can see find a binding energy of $E_b \approx 1.6\,\mathrm{K}$, corresponding to an energy scale of $E_b \approx 0.34\,\mathrm{meV}$.

The energy scale found as a result of fitting this data to the model in Eq. 4.1 is not realistic for the exciton binding energy, as it is well below the $5\,\mathrm{meV} - 20\,\mathrm{meV}$ range expected for excitons in GaAs [62]. In addition to the binding energy, the fit value for n_L is much larger than expected for such a low power laser. It is unlikely that such a large number of electron hole pairs could be generated by such low power excitation, due to the short recombination time for excitons.

In Fig. 4–6, it is noted that at high temperatures ($T \approx 2\,\mathrm{K}$) an almost "normal" quantum Hall trace returns. The Hall resistance once again has a linear slope in R_{xy}, without any curvature at high magnetic fields. Although the Landau level valleys are well defined, the Hall plateaus are still offset from their centre.

The transport measurements in Fig. 4–4 can be adjusted to remove the effect of the electron density's temperature dependence. Using the data in Fig. 4–5, the magnetic field is rescaled by

$$B' = \frac{n_0}{n\,(T)} \times B \tag{4.2}$$

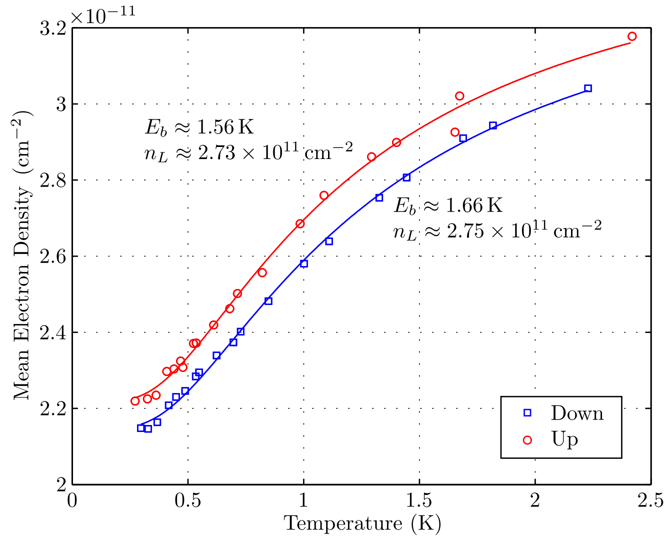

FIGURE 4–5: Demonstration of the temperature dependence of the quantum well's electron density. The solid lines are fits to the Boltzmann approximation in Eq. 4.1 with the given fitting parameters.

where n_0 is the electron density at the lowest temperature and $n(T)$ is the mean density for each sweep. In Fig. 4–7 one sees a much clearer picture of the temperature dependence of the additional for zero resistance states. This correction brings forth some subtle features present in the temperature dependence data.

Upon closer inspection of Fig. 4–7, one sees a very complex crossing behaviour of these additional zero resistance states in the temperature range from $T = 0.6\,\mathrm{K} - 1.4\,\mathrm{K}$. This behaviour appears to be present in the additional zero resistance states located near the Landau levels with odd filling factors. At high temperatures it is observed that, as expected, the odd filling factor Landau levels will close due to the loss of spin splitting. The interesting behaviour is that the additional states shift as the temperature evolution progresses which is not a result of the main density shift.

The arrow labelled (1) follows the path of a zero resistance state that begins near $\nu = 3$ and shows that as the temperature increases, the zero resistance gap crosses over into the $\nu = 2$ valley. A similar behaviour is found along the path of

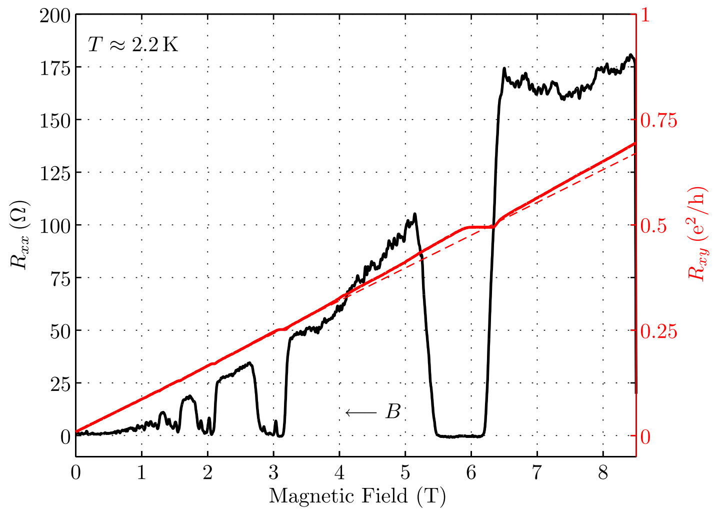

FIGURE 4–6: The offset in R_{xx} and R_{xy} is still present at higher temperatures. Only even number filling factors are present as the states due to spin splitting have closed at $T = 2.2\,\mathrm{K}$.

arrow (2), where the state transitions from $\nu = 5$ into $\nu = 4$. To take a closer look at this crossing over behaviour, Fig. 4–8 follows the temperature evolution of the structures on each side of arrow (1), which are labelled (γ) and (δ) in Fig. 4–7.

In Fig. 4–8(a), it is noted that the height of δ has a quite gradual decline with a small local maxima at $T \approx 0.8\,\mathrm{K}$. This follows the behaviour observed in the resistance map in Fig. 4–7, where δ declines into the $\nu = 2$ valley. In Fig. 4–8(b) the γ peak has a sharp incline at $T = 0.7\,\mathrm{K}$ and quickly saturates at $T \approx 0.8\,\mathrm{K}$. At this time, the origin of this crossing behaviour remains unclear and it will be the focus of future investigations.

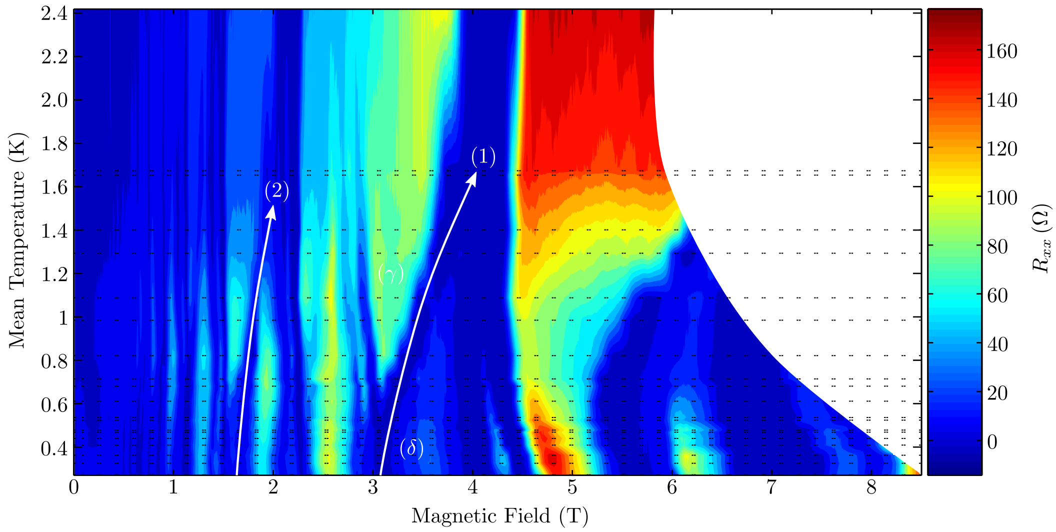

(a) B increasing

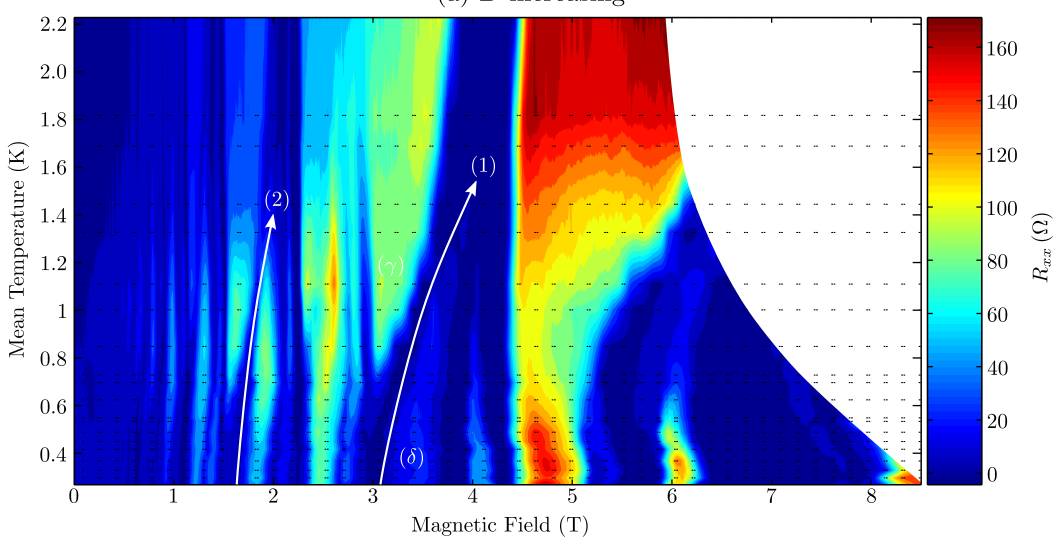

(b) B decreasing

Figure 4–7: B field sweeps (a) up and (b) down of the magnetoresistance's temperature dependence. The data in has been adjusted to compensate for changes in the well's electron density.

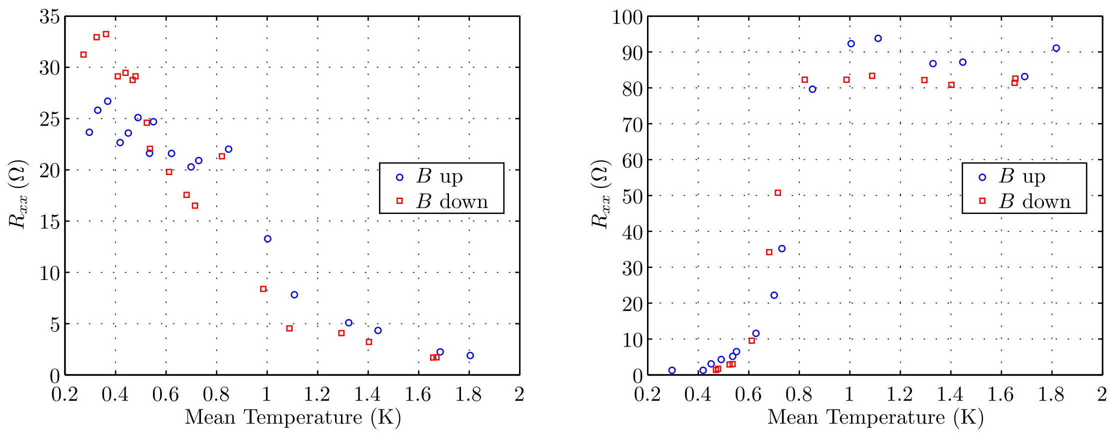

(a) Structure δ (b) Structure γ

Figure 4–8: Temperature dependence of the peak height of the structures (γ and δ) on either side of the crossing over gap. In (a) δ shows a slow decline with temperature, whereas in (b) γ demonstrates a sharp turn behaviour at $T = 0.7\,\mathrm{K}$.

4.4 Laser Power Dependence

In the previous section it was found that the behaviour of the GaAs/AlGaAs quantum well was heavily dependent on the temperature of the sample. One of the more complicated aspects of these experiments is that the light illuminating the sample, although very low power, is also heating the electrons in the 2DEG. In this section, an investigation will be conducted into the effect of changing the output power of the laser illuminating the sample while maintaining the sample as close to base temperature as possible. Although the temperature of the bulk sample will be near that of the base, the electrons in the quantum well are expected to undergo heating due to photoexcitation.

4.4.1 Reduced Laser Power

In the first part of this experiment, transport measurements were recorded for each step as the the laser driving current I_D was reduced from 40.05 mA to 20 mA. The procedure for acquiring these measurements was the same as for the temperature dependence except that at each driving current value the sample was maintained at low temperature. Fig. 4–9 shows that as the laser's power was reduced, the unknown zero resistance states begin to clear up, the slope of the Hall resistance returns to being constant and the density decreases to $n \approx 1.8 \times 10^{11}\,\mathrm{cm}^{-2}$ at $I_D = 20\,\mathrm{mA}$ ($P \approx 1.2\,\mu\mathrm{W}$).

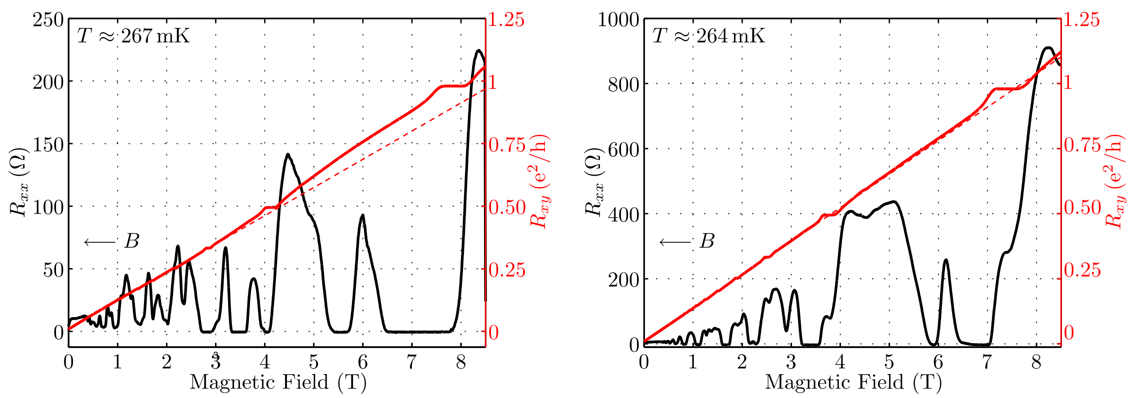

(a) $I_D = 37\,\mathrm{mA}$, $P \approx 8.6\,\mu\mathrm{W}$ (b) $I_D = 20\,\mathrm{mA}$, $P \approx 1.2\,\mu\mathrm{W}$

FIGURE 4–9: Transport measurements acquired as the illumination power was decreased. As the power was lowered, the structures of the unknown zero resistance states begins to degrade. At low power, the curvature of the Hall resistance has subsided.

4.4.2 No Illumination

At this point, a scheduled power outage required that the laser be turned off. A single transport measurement was completed before the power outage, but only in the low field range ($B < 4\,\mathrm{T}$), shown in Fig. 4–10(a). During the power outage, the sample warmed to $T \approx 5\,\mathrm{K}$ over a period of 12 h. After power had returned, the sample was cooled to base temperature ($T \approx 270\,\mathrm{mK}$) and a transport sweep was taken with the laser still off. Fig. 4–10 shows a comparison of the measurements taken before and after the sample was allowed to warm to $T \approx 5\,\mathrm{K}$.

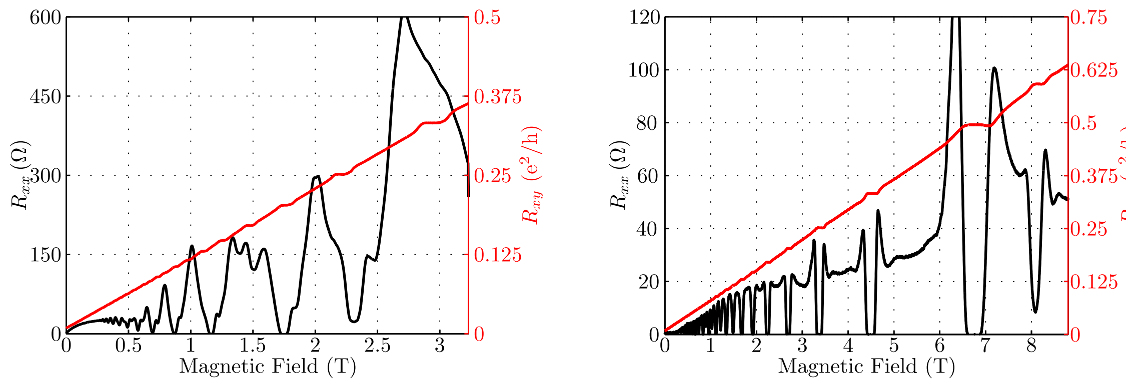

(a) (b)

Figure 4–10: Measurements of the sample's transport properties with no laser illumination. One can compare the state of the sample (a) before and (b) after it was allowed to warm to $T \approx 5\,\mathrm{K}$. The sample shows a very poor quality trace before the thermal cycle. After the sample was warmed, it appears to have had a complete recovery and all of the zero resistance states correspond to plateaus in the Hall resistance.

In Fig. 4–10(a), it is noted that the R_{xy} plateaus still do not coincide with the R_{xx} valleys. Remarkably, in Fig. 4–10(b) the sample appears to have had a complete recovery. The Hall resistance is once again linear and the plateaus fully coincide with the zero resistance states in R_{xx} and the system no longer exhibits a hysteretic behaviour. There are no unexplained zero resistance states present in the magnetoresistance. The electron density of the 2DEG has risen to $n \approx 3.3\times10^{11}\,\mathrm{cm}^{-2}$ which is actually *greater* than the density of the sample in its dark state ($n \approx 2.74 \times 10^{11}\,\mathrm{cm}^{-2}$).

4.4.3 Increased Laser Power

After this, the laser was turned on and the current was slowly increased to $I_D = 42\,\mathrm{mA}$ and measurements were acquired every $2\,\mathrm{mA}$ from $I_D = 42\,\mathrm{mA} - 50\,\mathrm{mA}$. At $42\,\mathrm{mA}$, the sample has returned to a state almost identical to the one taken at $40\,\mathrm{mA}$. As seen in Fig. 4–11(a), the zero resistance states in R_{xx} have returned along with the hysteretic behaviour in electron density and the offset between the R_{xy} plateaus and their coinciding R_{xx} valleys. As the current was increased to 48 mA, it is seen in Fig. 4–11(b) that the features of the transport measurements start to degrade in a similar fashion to those found at the high end of the temperature dependence data. The height of the gaps separating the zero resistance states begin to reduce and the spin split R_{xx} states (odd values of ν) start to close. This is strong evidence that the laser is causing significant electron heating in the 2DEG.

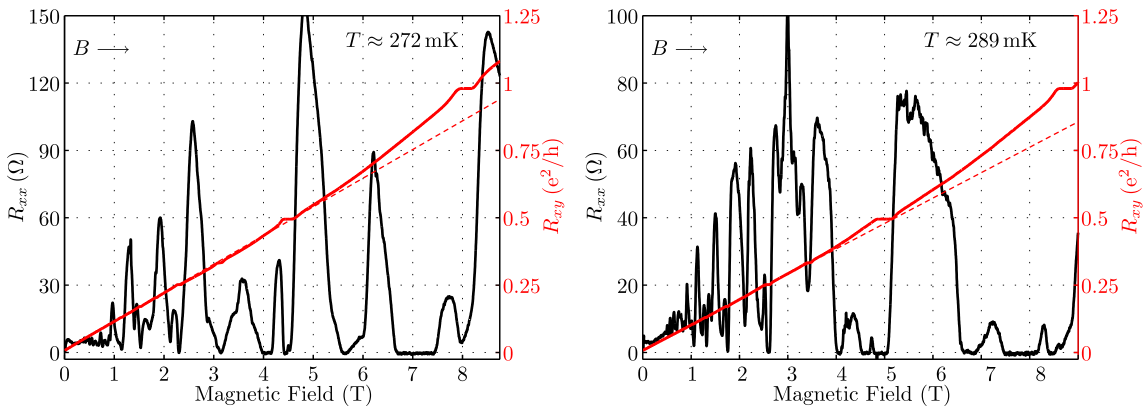

(a) $I_D = 42$ mA, $P \approx 16\,\mu$W

(b) $I_D = 48$ mA, $P \approx 58\,\mu$W

FIGURE 4–11: Demonstration of the effect that illumination power has on the quantum Hall system. At higher power, the zero resistance states begin to degrade as the electron heating becomes significant. Unlike the high temperature data in Fig. 4–6, even at high power there is still considerable curvature in the Hall resistance at high magnetic fields.

4.4.4 Electron Density

Similar to the temperature dependence experiments, a strong change in the electron density of the 2DEG was found as the power of the laser was varied. The mean electron density was again calculated using the centre of the Hall resistance plateaus. Fig. 4–12 summarizes the results of the laser power dependence discussed above.

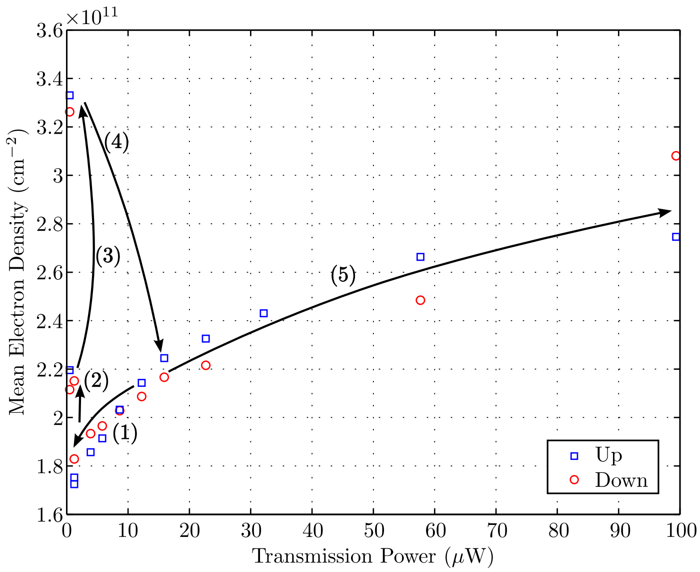

FIGURE 4–12: Electron density as a function of illumination power shining onto the surface of the GaAs/AlGaAs sample. Due to constraints beyond control, the data was acquired in the following order: (1) Laser power decreased. (2) Laser turned off. (3) Thermal cycle to $T \approx 5\,\mathrm{K}$. (4) Laser turned on. (5) Power increased to $100\,\mu\mathrm{W}$. After step (4) the data clearly follows the same trend as (1), suggesting the effect of the laser is well mastered.

In Fig. 4–12, a complex relationship emerges as a result of the laser illuminating the sample surface and interacting with the electrons in the quantum well. Under low power illumination, the sample density is depressed significantly lower than its dark state. As the power of the laser was increased, the density begins to rise as the electrons undergo heating which is consistent with the behaviour found in Fig. 4–5. As the power is further increased, the density begins to level off near that of its dark state. One of the most remarkable observations is that when the laser was turned off, the quantum Hall system was fully recovered after the sample was thermally cycled to $T \approx 5\,\mathrm{K}$. When the sample was once again illuminated, the electron density lowered along the same trend as discovered previously. The physical mechanism associated with this low energy scale remains to be further investigated.

4.5 Conclusions

This chapter presents the preliminary results of an investigation into the zero resistance state phenomena in the quantum Hall structure of a GaAs/AlGaAs quantum well under laser illumination. Under photoexcitation, it was observed that these states appear to be dependent on contact geometry used for conducting the measurements as the laser appears to locally modify the electron density of the quantum well [61]. A temperature dependence of the transport properties revealed that under constant illumination, the electron density of the 2DEG increases as a function of temperature following the behaviour of a Boltzmann two level system with energy gap $E_b \approx 1.6\,\mathrm{K}$. Normalizing the magnetoresistance curves to account for the density change reveals that some of the additional zero resistance states demonstrate a crossing over behaviour as the system's temperature was increased.

A complex behaviour in the sample's electron density also developed when the power of the light shining on the sample was varied. Under low power illumination, the density of 2DEG was significantly depressed in comparison to its dark state. As the power was increased, the electron density began to accrue, tending towards a saturation point near that of the dark state. The modifications caused by the laser to the quantum Hall state were found to be almost completely reversible under the thermal cycle conditions of $T \approx 5\,\mathrm{K}$.

CHAPTER 5

Conclusions

5.1 Summary

THE POTENTIAL OF USING THE NUCLEAR SPINS of GaAs as quantum information carriers was introduced in Chapter 1 and a number of topics related to their implementation were reviewed: GaAs/AlGaAs quantum well structures, the classical and integer quantum Hall effects, resistively detected nuclear magnetic resonance and dynamic nuclear polarization through optical pumping methods. In Chapter 2 the design and implementation of a cryogenic polarization controller that can output different polarization of light at the end of a standard single mode optical fiber was demonstrated. A model was devised to describe its operation with and without the presence of a magnetic field. In Chapter 3 the results of magneto-optical transport measurements show evidence of a direct relationship that exists between the polarization of the light illuminating the sample and the magnetoresistance of the $\nu = 1$ flank in a GaAs/AlGaAs quantum Hall system were reported. Dynamics experiments to determine the decay rates of the pumped states were also performed demonstrating evidence that this behaviour may be due to the dynamic polarization of the GaAs nuclear spins as a result of the circularly polarized photoexcitation. Chapter 4 reports on the observation of a complex series of zero resistance states in the quantum Hall structure under low power laser illumination. A thorough investigation into the sample's dependence on contact geometry, temperature and illumination power was presented and possible explanations were discussed.

5.2 Future Research

Although many of the results presented here show great progress towards the realization of GaAs as a quantum information carrier, further work is required to verify (i) that the power of the light exiting the fiber remains constant under all polarization conditions at low temperatures; (ii) that the nuclear spins are, in fact, being influenced by polarized photoexcitation; and (iii) the reproducibility of the laser induced zero resistance states. The following sections briefly explore each of these future research directions.

5.2.1 Nuclear Magnetic Resonance

In Chapter 3, a strong correlation was found between the ΔR_{xx} and the light's polarization [57]. In addition, the dynamics experiments found that the decay rates of these pumped states were in good agreement with those expected for the nuclear spin-lattice relaxation time of GaAs at $T \approx 270\,\mathrm{mK}$. To fully verify that these observations are a result of nuclear spin polarization, a coil must be installed around the sample to perform traditional resistively detected NMR experiments. While maintaining the sample in a circularly pumped state, the frequency of the radio-frequency oscillations applied to the NMR coil should be swept through the Larmor frequencies of the isotopes present in GaAs. If the nuclei are in fact polarized, sweeping through the Larmor resonance frequencies will destroy the induced nuclear polarization, resulting in a measurable change in R_{xx}. This would provide irrefutable proof that the system presented is dynamically polarizing the nuclear spins of the GaAs quantum well.

5.2.2 Polarization Controller

In order to validate the correlation between ΔR_{xx} and polarization, the effect of thermal changes on the system must be further investigated. A thorough characterization of the polarization controller's output at low temperatures will be required to ensure that the power of the light shining on to the sample is independent of polarization. The sensitivity of the quantum Hall state to small changes in the output power should also be investigated to determine the extent that could influence the system.

One of the key limitations to the current polarization controller design is its inability to measure the output power of the light shining on the sample. Although the intensity of the back-reflected light is directly proportional to the intensity of the fiber's output, it cannot provide an absolute measure of the output power because it is dependent on a number of other variables. One proposed solution is to install near the sample surface a bolometer that is exposed to some of the light originating from the fiber. A bolometer is typically a temperature sensitive resistor that is heated by incoming radiation and cooled by the thermal conduction of its electrical wires [63–68]. Once calibrated, a bolometer mounted near the sample would provide an in situ method of measuring the absolute output power of the light exiting the fiber. Additionally, this could act as a means of correcting small misalignment of the optical system without requiring the system to be warmed to room temperature.

5.2.3 Laser Induced Phenomena

Although the investigation presented in Chapter 4 has resulted in a number of interesting and astonishing observations, the true origin of these laser induced zero resistance states presently remains unclear. Future experiments are planned using a small Hall bar sample made from the same wafer as that used in these experiments, as shown in Fig. 5–1.

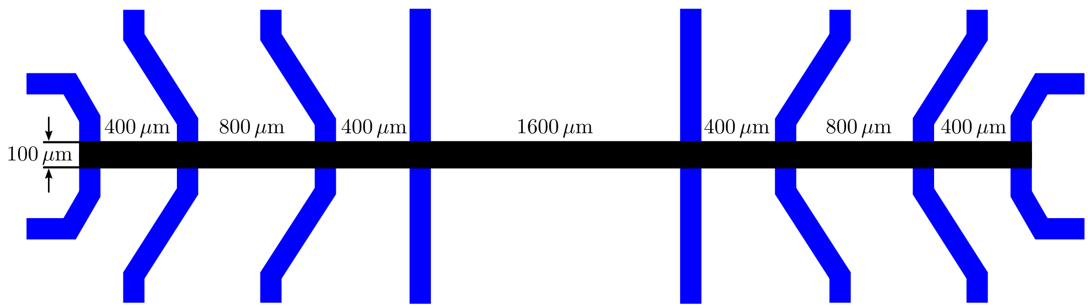

FIGURE 5–1: Illustration of a Hall bar sample with a width of 100 μm. The contact arms, shown in blue, are patterned using standard photolithography techniques.

Using the Hall bar should help to eliminate some of the uncertainty related to the size of the quantum well sample. The smaller area Hall bar may help reduce, to some extent, the inhomogeneity of the quantum well's electron density while under illumination. Similar measurements to those presented here will be conducted to determine the reproducibility of the behaviour demonstrated by additional zero resistance states as a function temperature and of illumination power. It is hoped that these future endeavours will help unravel the origins of these laser induced zero resistance phenomena.

APPENDIX A

Further Details

A.1 Contact Quality Circuit

The circuit shown in Fig. A–1 was used to verify the quality of each contact on the sample once it was cooled to liquid Helium temperatures ($T = 4.2\,\mathrm{K}$). Each contact was connected as shown and the differential voltage was measured across the $10\,\mathrm{k\Omega}$ resistor to determine the current flowing through the contact on the sample. A "good" contact will have current flow of $I \approx 60\,\mathrm{nA} - 70\,\mathrm{nA}$.

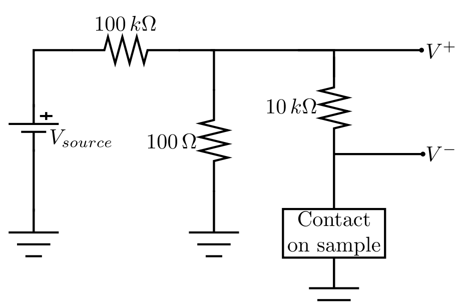

FIGURE A–1: Diagram of the circuit used to test the quality of the sample contacts.

A.2 Sample Growth Data

EPI-A GROWTH SHEET **EA0746**

SAMPLE ID: EA0746 **OBJECTIVE:** High Mobility Structure
DATE: 09-May-01 **CUSTOMER:** Lilly,M
GROWER: Reno, J. **MATERIAL:** GaAs, AlGaAs

Structure

#	Material	Thickness	Dopant	Density	Temp.	SL	Comment
1	GaAs	10.0 nm	undoped		635 °C		Cap
2	AlGaAs	98.0 nm	undoped		635 °C		24%
3	AlAs	2.0 nm	undoped		635 °C		7ML Upper Clad
4	GaAs	2.3 nm	undoped		580 °C		8ML Upper QW
5	delta-dope	0.0 nm	Si (n)	1.00E+12	580 °C		Upper Delta
6	GaAs	0.6 nm	undoped		635 °C		2ML Upper QW
7	AlAs	2.0 nm	undoped		635 °C		7ML Upper Clad
8	AlGaAs	75.0 nm	undoped		635 °C		24% Upper Setback
9	GaAs	30.0 nm	undoped		635 °C		QW
10	AlGaAs	95.0 nm	undoped		635 °C		24% Lower Setback
11	AlAs	2.0 nm	undoped		635 °C		7 ML Lower Clad
12	GaAs	2.3 nm	undoped		580 °C		8ML Lower QW
13	delta-dope	0.0 nm	Si (n)	1.00E+12	580 °C		Lower Delta
14	GaAs	0.6 nm	undoped		635 °C		2ML Lower QW
15	AlAs	2.0 nm	undoped		635 °C		7ML Lower Clad
16	AlGaAs	98.0 nm	undoped		635 °C		24%
17	GaAs	3.0 nm	undoped		635 °C	[x300	Smoothing SL
18	AlGaAs	10.0 nm	undoped		635 °C	]	
19	GaAs	100.0 nm	undoped		635 °C		Buffer

Substrate Information

Ingot:	G079K3400
Slice:	
Material:	GaAs
Orientation:	(100)
Thickness:	625 μm
Diameter:	3"
Type:	undoped
Vendor:	AXT

Source Information

Source	Temp °C	Flux	G.R. ML/s	Rheed	UFG	Comment
Al7	1155.5		0.243	Yes	Yes	
As2_Va	200.0		1.980	Yes	Yes	
As2C	650.0		0.000	No	Yes	
As2X	390.0		0.000	No	Yes	
Ga3	1171.5		0.771	Yes	Yes	GaAs, 24% AlGaAs
Ga9	1088.5		0.198	Yes	Yes	55.1% AlGaAs
Rotate	-15.0		0.000	No	Yes	
Rotate	-5.0		0.000	No	Yes	Buffer
Si	1212.0		0.000	No	Yes	

Notes and Comments:

Duplicate of EA0745 w/ temperature drops around the delta dopes.

1

FIGURE A–2: Molecular beam epitaxy growth data sheet for the wafer EA0746. The GaAs/AlGaAs quantum well sample used for all experiments described in this thesis was from this wafer.

APPENDIX B

Software Source Code

B.1 Experimental Analysis of $\alpha - \beta$ Maps

`AlphaBetaImport.m`

```
% This program takes the output files from BackMotorOptics.vi v2.0 and parses
% them for the necessary information to generate a contour plot.  It relies
% on a standardized naming scheme for the files that the software uses.
%    Format:      (QWP1)_(QWP2).lvm
%    Example:     50_142.lvm
% Also required is a constant QWP change difference between each of the
% file slices ('degree' variable).  The default is 5 degrees.

% Simply write in the directory containing the data files, change the date
% and field values, and set the QWP limits/ increment value.
clc;
clear;

%%%%%%%%%%%%% START OF CONFIGURATION %%%%%%%%%%%%%
Directory = '/Data/2007-03-07/backreflection/'; % Data files.
Date = 'March 7, 2007';      % Date of sweep, for plot title.
field = 0;                   % B field, for plot title.
fontsize = 12;               % Fontsize for the plot axes
savefiles = 1;               % Save the plots and analyzed data?  (YES=1, NO=0)
QWP1 = [ 70 125];            % Range of the first QWP. (Format: [start end])
%%%%%%%%%%%%%% END OF CONFIGURATION %%%%%%%%%%%%%%

degree = 5;  %Number of degrees between each data set.

QWP2 = QWP1+92;
numfile = (QWP1(2) - QWP1(1))/degree;   %Number of files to import

for j = 1:numfile+1
    filename = fullfile(Directory,strcat(num2str(QWP1(1)+(j-1)*degree),'_',num2str(QWP2(1)+(j-1)*degree),'.lvm'));
    fid = fopen(filename);
    Data(:,:,j) = textscan(fid, '%f %f %f','headerlines', 21);
    fclose(fid);
    Z(:,j)  = cell2mat(Data(:,2,j));
end
% Extract the axes labels
Y = cell2mat(Data(:,1,2))/64;
```

```
X= QWP1(1):degree:QWP1(2);

figure(1)
contourf(X,Y,Z,20,'LineStyle','none')
xlabel('\alpha (Degrees)','FontSize',fontsize)
ylabel('\beta (Degrees)','FontSize',fontsize)
title(['Backreflection \alpha - \beta Map, ', Date, ',  Field = ', num2str(field),' T'],'FontSize',fontsize)
colorbar
grid on

% Force proper tick locations on the plots.
set(gca,'XTick',QWP1(1):10:QWP1(2),'XTickLabel',QWP1(1):10:QWP1(2))
set(gca,'YTick',0:20:180,'YTickLabel',0:20:180)

% Format the data into a single matrix which can be easily imported into
% Origin if you prefer to use origin to plot the contour.
% Simply uncomment the following and run:
if savefiles == 1
    OriginOut(2:length(Y)+1,1) = Y;
    OriginOut(1,2:numfile+2) = X;
    OriginOut(2:length(Y)+1,2:numfile+2) = Z;
    csvwrite(strcat(Directory,'AlphaBetaMap-',Date,'.csv'),OriginOut)

% Generate and save images in 3 convenient formats.
    [filepath,filename,ext,versn] = fileparts(Directory);
    saveas(gcf,fullfile(filepath,strcat(filename,'AB_Map.pdf')));
    saveas(gcf,fullfile(filepath,strcat(filename,'AB_Map.fig')));
    saveas(gcf,fullfile(filepath,strcat(filename,'AB_Map.png')));
end
```

B.2 Simulation of $\alpha - \beta$ Maps and Faraday Rotation

`simulate.m`

```
% This function is used to generates the simulation of the polarization
% controller's back-reflection intensity.
%
% Syntax: simulate(plate, faraday, fiber, bfield)
%
% where    bfield = magnetic field strength
%          plate = struct('HWPmin',HWPmin,'HWPmax',HWPmax,'QWPmin',QWPmin,'QWPmax',QWPmax);
%          faraday = struct('lambda0',lambda0','length',Blength);
%          fiber =  struct('thet',thet,'phi',phi,'thi',thi);
%
% Last modified: October 2007
% Copyright 2007 Jonathan M. Buset
function SimOut=simulate(plate, faraday, fiber, bfield)
%     Loop over the HWP (beta)
for e = plate.HWPmin:5:plate.HWPmax
%     Loop over the first QWP (alpha)
    for f = plate.QWPmin:5:plate.QWPmax
        a=1*f*pi/180;
        b=-1*(e)*pi/180;
        c=1*(f+180)*pi/180;

        % Generate polarization
        amplitude = jones(a,b,c,plate, faraday, fiber, bfield);
        % Calculate the intensity
        Output((e/5)-(plate.HWPmin/5)+1,(f/5)-(plate.QWPmin/5)+1)= amplitude'*amplitude;
    end %f (QWP)
```

```
end % e (HWP)
SimOut = Output;
```

jones.m

```
% This function performs the Jones matrix calculations of the light's
% polarization as it travels through the polarization controller.
%
% Syntax: jones(a, b, c, plate, faraday, fiber, bfield)
%
% where    a,b,c = waveplate angles
%          faraday = faraday rotation parameters
%          fiber = optical fiber parameters
%          bfield = magnetic field strength (T)
%
% Last modified: October 2007
% Copyright 2007 Jonathan M. Buset
function jones_amplitude = jones(a, b, c, plate, faraday, fiber, bfield)
% First 1/4 waveplate
Q = 1/(sqrt(2))*[1-i*cos(2*a)  -i*sin(2*a) ;
                 -i*sin(2*a)    1+i*cos(2*a)];
% Half waveplate
H = [-i*cos(2*b)    -i*sin(2*b) ;
     -i*sin(2*b)    i*cos(2*b) ];
% Second 1/4 waveplate
Q2 = 1/(sqrt(2))*[1-i*cos(2*c)      -i*sin(2*c) ;
                  -i*sin(2*c)        1+i*cos(2*c)];
% Standard 90 degrees quarter waveplate
QWP = 1/(sqrt(2))*[1-i*cos(-(pi/2))  -i*sin(-(pi/2)) ;
                   -i*sin(-(pi/2))    1+i*cos(-(pi/2))];

% For the backreflected signals, the transformation matrices are simply in
% inverse matrices of the forward transformations.
Qi=inv(Q);
Hi=inv(H);
Q2i=inv(Q2);
% Initial signal, consisiting of vertically linearly polarized light.
Signal = [0; 1];

% Faraday effect due to the magnetic field affecting the laser light as
% it travels through the B-field.  This changes the resulting
% polarization.
Gamma = faraday.verdetL*bfield;
R=[exp(i*Gamma) 0 ; 0 exp(-i*Gamma)];

% The following is the Transformation matrix of the fiber
F=[exp(i*fiber.phi)*cos(fiber.thet)  -exp(-i*fiber.psi)*sin(fiber.thet);
   exp(i*fiber.psi)*sin(fiber.thet)  exp(-i*fiber.phi)*cos(fiber.thet)];

% D3 is the light exiting the fiber.
D3= R * F * Q2 * H * Q * Signal;

% Assumption: The faraday effect part happens at the end of the laser
% where there are no bends so the Jones matrix may just be tacked on
jones_amplitude=[1 0;0 0] * Qi * Hi * Q2i * inv(F) * R' * conj(D3);
```

B.3 Analysis of B Field Sweeps

BFieldSweep3.m

```
% This program takes the data output by "NML Acquisition Software", parses
% it, scales the values according to the provided parameters below,
```

```
% displays a plot, and outputs an analyzed data file and parameter list.
%
% Last modified: May 2008
% Copyright 2008 Jonathan M. Buset
clc;
clear;

%%%%%%%%%%%%%%%%%%%%%%%%%%%%%%%%%%%%%%%%%%%%%%%%%%%%%%%%%%%%%%%%%%%%%%
%%%%%%%%%%%%%%%%%%%%%% DEFINE EXPERIMENT PARAMETERS %%%%%%%%%%%%%%%%%%%%%%
filename = '/Data/2008-04-05/YbPTgB laser=48mAup.001';
num_skip = 17;        % The number of header lines to skip
preamp = 1;           % Pre-amplifier Gain
LIsens1 = 10;         % (V)
LIsens2 = 5000e-6;    % (V)
Iapplied = 100e-9;    % (A)
save_files = 0;       % Save plots and data files?
save_plots = 0;
%%%%%%%%%%%%%%%%%%%%%%%%%%%%%%%%%%%%%%%%%%%%%%%%%%%%%%%%%%%%%%%%%%%%%%
%%%%%%%%%%%%%%%%%%%%%% DO NOT EDIT BELOW THIS LINE %%%%%%%%%%%%%%%%%%%%%%
%%%%%%%%%%%%%%%%%%%%%%%%%%%%%%%%%%%%%%%%%%%%%%%%%%%%%%%%%%%%%%%%%%%%%%

% Format a nice title/date string from the filename.
[titlestring datestring] = filename_format(filename);
[PATHSTR,NAME,EXT] = fileparts(filename);
% Extract contacts as first part of filename
contacts = strtok(NAME, ' ');

% Build structure for all the experiment parameters
param = struct('filename',filename,'preamp',preamp,'LIsens1',LIsens1,'LIsens2',LIsens2,'Iapplied',Iapplied,'contacts',contacts);

% Load the raw data from the text file.
Data = load_data(filename,6,num_skip);  % load the data file
% Perform scaling and calculations
FinalData= dataBfield(Data,param);
clear Data;

% Fit the low field data of the hall resistance. (B<2T)
he2 = 6.626068*10^(-34) / (1.60217646*10^(-19))^2;
B_fit = find(FinalData(:,1) < 2);
fit = polyfit(FinalData(B_fit,1),FinalData(B_fit,3).*he2^(-1),1);

%%%%%%%%%%%%%%%%%%%%%%%%%%%%%%%%%%%%%%%%%%%%%%%%%%%%%%%%%%%%%%%%%%%%%%
%%%%%%%%%%%%%%%%%%%%%% FORMAT PLOTS FOR DISPLAY %%%%%%%%%%%%%%%%%%%%%%
%%%%%%%%%%%%%%%%%%%%%%%%%%%%%%%%%%%%%%%%%%%%%%%%%%%%%%%%%%%%%%%%%%%%%%
% Rxx and Rxy plots together:
f(1) = figure(2);
[A H] = plotBfield({'B','rxxO_in','B','rxy2'},FinalData,'plotyy');
title(titlestring)
hold on
% Add a fit line to the Hall resistance
line(FinalData(:,1),polyval(fit,FinalData(:,1)),'Color','r','LineStyle','--','Parent',A(2),'LineWidth',1);
hold off

% Rxx just plot:
% f(1) = figure(1);
plotBfield({'B','rxxO_in'},FinalData,'plot')
title(titlestring)
xlim([0 9])
%%%%%%%%%%%%%%%%%%%%%%%%%%%%%%%%%%%%%%%%%%%%%%%%%%%%%%%%%%%%%%%%%%%%%%
%%%%%%%%%%%%%%%%%%%%%% WRITE ANALYZED DATA TO FILE %%%%%%%%%%%%%%%%%%%%%%
%%%%%%%%%%%%%%%%%%%%%%%%%%%%%%%%%%%%%%%%%%%%%%%%%%%%%%%%%%%%%%%%%%%%%%
```

```
save_dir = fullfile(PATHSTR,strcat(NAME,EXT,'(analyzed)/'));
if save_files == 1
    if isdir(save_dir) == 0
        mkdir(save_dir);
    end

    f1 = fullfile(save_dir,strcat(NAME,EXT,'_analyzed.csv'));
    fid1 = fopen(f1,'w');
    fprintf(fid1,'%s\n','***** Header *****');
    fprintf(fid1,'%s,%s\n', 'Date of Analysis',date);
    fprintf(fid1,'%s,%s\n', 'Data Filename',filename);
    fprintf(fid1,'%s,%s\n', 'Contacts',contacts);
    fprintf(fid1,'%s,%.0f\n', 'Preamp Gain',preamp);
    fprintf(fid1,'%s,%.0f\n', 'Lock-in Sensitivity (uV) CH1',LIsens1/1e-6);
    fprintf(fid1,'%s,%.0f\n', 'Lock-in Sensitivity (uV) CH2',LIsens2/1e-6);
    fprintf(fid1,'%s,%.0f\n', 'Applied Current (nA)',Iapplied/1e-9);
    fprintf(fid1,'%s\n','***** End of Header *****');
    fprintf(fid1,'%s,%s,%s,%s,%s,%s,%s\n','Field(T)','R_1(Ohm)','R_2(Ohm)','R_1↘
    →(V)','R_2(V)','Temp(K)','Timestamp(s)');
    fprintf(fid1,'%f,%f,%f,%e,%e,%f,%f\n',FinalData(:,[1 2 3 6 7 9 10])');
    fclose(fid1);
end

if save_plots == 1;
    if isdir(save_dir) == 0
        mkdir(save_dir);
    end
    for K = 1:length(f)
    saveas(f(K),fullfile(save_dir,strcat(NAME,EXT,'_',num2str(f(K)),'.png')));
    saveas(f(K),fullfile(save_dir,strcat(NAME,EXT,'_',num2str(f(K)),'.fig')));
    end
end
```

dataBfield.m

```
% Scales the input data according to the experiment parameters and output
% in a number of different convenient formats for plotting.
%
% Syntax: dataBfield(Data, parameters)
%
% Last modified: April 2008
% Copyright 2008 Jonathan M. Buset
function DataOut = dataBfield(Data, p)

% Do scaling calculations
B=Data(:,1);
R1_V = (Data(:,2).*(p.LIsens1/10))./p.preamp;
R2_V = (Data(:,3).*(p.LIsens2/10))./p.preamp;

% Convert R to Ohms
R1_Ohm = R1_V/p.Iapplied;
R2_Ohm = R2_V/p.Iapplied;

% Scale temperature according to given resistor calibration
TempK = TempC_K(Data(:,4));
meanTemp = mean(TempK)

% First derivative of R
dR1 = diff(moving_avg(R1_Ohm,9));
dR2 = diff(moving_avg(R2_Ohm,9));

R1_Ohm = moving_avg(R1_Ohm,9);
% Make the last value the same as second last, so the vector is the same
```

```
% length as the others.  This is a decent approximation, as the last points
% aren't usually used for anything.
dR1(length(dR1)+1) = dR1(length(dR1));
dR2(length(dR2)+1) = dR2(length(dR2));

% Calculate the filling factor (nu)
h=6.62606876E-34;
e=1.602176462E-19;
nu = 1./(R1_Ohm.*((e^2)/h));

% Group analyzed data for output to file.
DataOut = [ B  R1_Ohm    R2_Ohm  dR1  dR2   R1_V    R2_V     nu      TempK  Data↘
→(:,6)];
```

plotBfield.m

```
function [AX H] = plotBfield(xy, Data, plottype)
% This function takes the descriptors of the data sets to be plotted as
% strings, along with options to plot error bars.  It customizes the output
% plot depending on the type of data required.
%
% Syntax: plotBfield(xy, Data, plottype)
%
% where y = {'B','rxxO_in','1/B','rxyO'}
%       xparams = struction created in calling code
%       Data = pre-analyzed data, for plotting
%
% Last modified: February 2008
% Copyright 2008 Jonathan M. Buset
%%%%%%%%%%%%%%%%%%%%%%%%%%%%%%%%%%%%%%%%%%%%%%%%%%%%%%%%%%%%%%%%%%%%%%%%%%%%
rxx_in_colour   = 'k';      % Color of Rxx data (in phase)
rxx_out_colour  = 'b';      % Color of Rxx data (out of phase)
rxy_colour      = 'r';
drxy_colour     = 'b';
temp_colour     = 'r';      % Color of Temperature data
nu_colour       = 'm';
legend_location = 'Best';   % Location of the legend on all of the plots
fontsize        = 12;
plot_ydivisions = 4;        % Number of divisions of the y-axes.
%%%%%%%%%%%%%%%%%%%%%%%%%%%%%%%%%%%%%%%%%%%%%%%%%%%%%%%%%%%%%%%%%%%%%%%%%%%%
%%%%%%%%%%% END OF VARIABLES, DO NOT EDIT BELOW THIS LINE %%%%%%%%%%%%%%%%%%%
%%%%%%%%%%%%%%%%%%%%%%%%%%%%%%%%%%%%%%%%%%%%%%%%%%%%%%%%%%%%%%%%%%%%%%%%%%%%
he2 = 6.626068*10^(-34) / (1.60217646*10^(-19))^2;

% Force a default plot type.
if nargin == 2
    plottype = 'plotyy';
end

if length(xy) == 2
    numplots = 1;
    x(1) = xy(1);
    y(1) = xy(2);
    plottype = 'plot';      % Force a single y-axis plot
elseif length(xy) == 4
    numplots = 2;
    x(1:2) = xy(1:2:3);
    y(1:2) = xy(2:2:4);
    % Determine if the two x-axes are the same.
    if strcmp(x(1),x(2))
        same_x = 1;
    else
        same_x = 0;
```

```
    end
else
    error('Wrong number of x-y inputs.')
end
% Don't muck with the y-axis limits (Default unless temperature or dR/dt)
limit_y = 0;

% Define structures for plot styles
rxxO_in = struct('ydata', 2, 'yscale', 1, 'string', 'R_{xx} (\Omega) [In]', 'colour', rxx_in_colour, 'linestyle','-');
rxxO_out = struct('ydata', 3, 'yscale', 1, 'string', 'R_{xx} (\Omega) [Out]', 'colour', rxx_out_colour, 'linestyle','-');
rxy1 = struct('ydata', 2, 'yscale', 1e-3, 'string', 'R_{xy} (k\Omega) [Hall Resistance]', 'colour', rxy_colour, 'linestyle','-');
rxy2 = struct('ydata', 3, 'yscale', he2^(-1), 'string', 'R_{xy} (e^2/h)', 'colour', rxy_colour, 'linestyle','-');
drxy1 = struct('ydata', 4, 'yscale', 1, 'string', 'dR_{xy}/dt (\Omega/s)', 'colour', drxy_colour, 'linestyle','-');
drxy2 = struct('ydata', 5, 'yscale', 1, 'string', 'dR_{xy}/dt (\Omega/s)', 'colour', drxy_colour, 'linestyle','-');
rxxV_in = struct('ydata', 6, 'yscale', 1e6, 'string', 'R_{xx} (\muV) [In]', 'colour', rxx_in_colour, 'linestyle','-');
rxxV_out = struct('ydata', 7, 'yscale', 1e6, 'string', 'R_{xx} (\muV) [Out]', 'colour', rxx_out_colour, 'linestyle','-');
nu = struct('ydata', 8, 'yscale', 1, 'string', '\nu [Filling Factor]', 'colour', nu_colour, 'linestyle','-');
temp = struct('ydata', 9, 'yscale', 1e3, 'string', 'Temperature (mK)', 'colour', temp_colour, 'linestyle','-');

for k = 1:numplots
    % match the y-axis data structure with the input data type
    if strcmp(y(k),'rxxO_in')
        ax(k) = rxxO_in;
    elseif strcmp(y(k),'rxxO_out')
        ax(k) = rxxO_out;
    elseif strcmp(y(k),'rxxV_in')
        ax(k) = rxxV_in;
    elseif strcmp(y(k),'rxxV_out')
        ax(k) = rxxV_out;
    elseif strcmp(y(k),'rxy1')
        ax(k) = rxy1;
    elseif strcmp(y(k),'rxy2')
        ax(k) = rxy2;
        limit_y = [k k];
    elseif strcmp(y(k),'drxy1')
        ax(k) = drxy1;
        limit_y = [1 k];
    elseif strcmp(y(k),'drxy2')
        ax(k) = drxy2;
        limit_y = [1 k];
    elseif strcmp(y(k),'nu')
        ax(k) = nu;
    elseif strcmp(y(k),'temp')
        ax(k) = temp;
        limit_y = [2 k];
    else
        error('Invalid plot input data type (%s).', y(k))
    end
    % Calcaulate/generate the correct x-axis stuff
    if strcmp(x(k),'B')
        xdata(:,k) = Data(:,1);
        xparams(k) = struct('label', 'Magnetic Field (Tesla)','limits', [min(xdata(:,k)) max(xdata(:,k))]);
```

```
%           xparams(k) = struct('label', 'Magnetic Field (Tesla)','limits', [3 5]);
    elseif strcmp(x(k),'1/B')
        xdata(:,k) = 1./Data(:,1);
        xparams(k) = struct('label', 'B^{-1} (1/Tesla)','limits', [min(xdata(:,k)) 1]);
    elseif strcmp(x(k),'time')
        xdata(:,k) = Data(:,10);
        xparams(k) = struct('label', 'Time (s)','limits', [min(xdata(:,k)) max(xdata(:,k))]);
    else
        error('Error:xaxis','Wrong input for xaxis data type. \nValid options: "B", "1/B", "time"');
    end
end

if strcmp(plottype, 'plotyy')
    [AX,H(1),H(2)] = plotyy(xdata(:,1),ax(1).yscale*Data(:,ax(1).ydata),xdata(:,2),ax(2).yscale*Data(:,ax(2).ydata),'plot');
    for j = 1:2
        set(get(AX(j),'YLabel'),'String',ax(j).string,'Color',ax(j).colour)
        set(H(j),'Color',ax(j).colour,'LineStyle',ax(j).linestyle,'LineWidth',1)
        set(AX(j),'YColor',ax(j).colour,'XLim',xparams(j).limits)

        % Set the x- and y-axis ticks so that they line up
        if limit_y(1) == 1 && j == limit_y(2);
            ymax = ceil(max(Data(30:length(Data)-30,ax(j).ydata))*1)*ax(j).yscale/1;
            ymin = floor(min(Data(30:(length(Data)-30),ax(j).ydata))*1)*ax(j).yscale/1;
            ylimits = [ymin ymax];
            set(AX(j),'YLim',ylimits);
        elseif limit_y(1) == 2 && j == limit_y(2);
            ymax = ceil(max(Data(:,ax(j).ydata))*ax(j).yscale);
            ymin = floor(min(Data(:,ax(j).ydata))*ax(j).yscale);
            ylimits = [ymin ymax];
            set(AX(j),'YLim',ylimits);
        else
            ylimits = get(AX(j),'YLim');
        end
        yinc = (ylimits(2)-ylimits(1))/plot_ydivisions;
        set(AX(j),'YTick',[ylimits(1):yinc:ylimits(2)]);
    end

    if same_x == 0
        % Colourize the x-axis & labels if they are not the same.
        % Otherwise, they will stay the default.
        for k = 1:2
            set(get(AX(k),'XLabel'),'String',xparams(k).label,'Color',ax(k).colour,'FontSize',fontsize)
        end
        set(AX(1),'XAxisLocation','bottom','YAxisLocation','left', 'XColor',ax(1).colour,'YColor',ax(1).colour,'FontSize',fontsize);
        set(AX(2),'XAxisLocation','top','YAxisLocation','right', 'XColor',ax(2).colour,'YColor',ax(2).colour,'FontSize',fontsize);
    else
        xlabel(xparams(1).label,'FontSize',fontsize)
    end

    % Stuff that always gets set, no matter what the data type is
    set(get(AX(1),'Ylabel'),'FontSize',fontsize);
    set(get(AX(2),'Ylabel'),'FontSize',fontsize);
```

```
%       legend([H(1) H(2)],ax(1).string,ax(2).string,'Location',legend_location)

elseif strcmp(plottype, 'plot')
    if numplots == 1
        H = plot(xdata,ax(1).yscale*Data(:,ax(1).ydata),strcat(ax(1).colour,ax↘
        →(1).linestyle));
        ylabel(strcat(ax(1).string));
    else
        H = plot(xdata,ax(1).yscale*Data(:,ax(1).ydata),strcat(ax(1).colour,ax↘
        →(1).linestyle),...
                xdata,ax(2).yscale*Data(:,ax(2).ydata),strcat(ax(2).colour,ax↘
                →(2).linestyle));
        ylabel(strcat(ax(1).string,' / ',ax(2).string));
        legend(ax(1).string,ax(2).string,'Location',legend_location);
    end
    AX = gca;

    xlim(xparams(1).limits);
    xlabel(xparams(1).label,'FontSize',fontsize);
    set(get(AX,'Ylabel'),'FontSize',fontsize);
    set(get(AX,'Xlabel'),'FontSize',fontsize);
end

% Stuff that always gets set, no matter what the data type is
grid on
```

References

[1] S. A. Wolf et al., Science **294**, 1488 (2001).

[2] J. R. Petta, A. C. Johnson, C. M. Marcus, M. P. Hanson, and A. C. Gossard, Phys. Rev. Lett. **93**, 186802 (2004).

[3] M. N. Leuenberger, D. Loss, M. Poggio, and D. D. Awschalom, Phys. Rev. Lett. **89**, 207601 (2002).

[4] G. Yusa, K. Muraki, K. Takashina, K. Hashimoto, and Y. Hirayama, Nature **434**, 1001 (2005).

[5] T. R. Carver and C. P. Slichter, Phys. Rev. **102**, 975 (1956).

[6] G. Salis et al., Phys. Rev. Lett. **86**, 2677 (2001).

[7] A. K. Paravastu et al., Phys. Rev. B **69**, 075203 (2004).

[8] A. Abragam, *Principles of Nuclear Magnetism*, Monographs on Physics, Claredon Press, Oxford, 1961.

[9] F. Meier and B. P. Zakharchenya, editors, *Optical Orientation*, volume 8 of *Modern Problems in Condensed Matter Sciences*, Elsevier, 1984.

[10] A. Y. Cho and J. R. Arthur, Prog. Solid State Chem. **10**, 157 (1975).

[11] S. Adachi, J. Appl. Phys. **58**, R1 (1985).

[12] H. Bruus and K. Flensberg, *Many-Body Quantum Theory in Condensed Matter Physics*, Oxford Graduate Texts, Oxford University Press, 2004.

[13] N. W. Ashcroft and D. N. Mermin, *Solid State Physics*, Thomson Learning, Toronto, 1976.

[14] D. Neamen, *Semiconductors Physics and Devices*, McGraw-Hill, New York, NY, 3rd edition, 2003.

[15] C. Kittel, *Introduction to Solid State Physics*, Wiley, 8th edition, 1996.

[16] E. H. Hall, Am. J. Math. **2**, 287 (1879).

[17] D. K. Cheng, *Field and Wave Electromagnetics*, Addison-Wesley Series in Electrical Engineering, Addison-Wesley, Reading, Mass., 2nd edition, 1989.

[18] K. v. Klitzing, G. Dorda, and M. Pepper, Phys. Rev. Lett. **45**, 494 (1980).

[19] R. B. Laughlin, Phys. Rev. B **23**, 5632 (1981).

[20] H. L. Stormer, Rev. Mod. Phys. **71**, 875 (1999).

[21] H. L. Stormer, D. C. Tsui, and A. C. Gossard, Rev. Mod. Phys. **71**, S298 (1999).

[22] D. C. Tsui, H. L. Stormer, and A. C. Gossard, Phys. Rev. Lett. **48**, 1559 (1982).

[23] F. Bloch, Phys. Rev. **70**, 460 (1946).

[24] E. M. Purcell, H. C. Torrey, and R. V. Pound, Phys. Rev. **69**, 37 (1946).

[25] S. E. Barrett, R. Tycko, L. N. Pfeiffer, and K. W. West, Phys. Rev. Lett. **72**, 1368 (1994).

[26] S. E. Barrett, G. Dabbagh, L. N. Pfeiffer, K. W. West, and R. Tycko, Phys. Rev. Lett. **74**, 5112 (1995).

[27] D. Rugar, R. Budakian, H. J. Mamin, and B. W. Chui, Nature **430**, 329 (2004).

[28] M. Dobers, K. v. Klitzing, J. Schneider, G. Weimann, and K. Ploog, Phys. Rev. Lett. **61**, 1650 (1988).

[29] W. Desrat et al., Phys. Rev. Lett. **88**, 256807 (2002).

[30] G. Gervais et al., Phys. Rev. Lett. **94**, 196803 (2005).

[31] L. A. Tracy, J. P. Eisenstein, L. N. Pfeiffer, and K. W. West, Phys. Rev. Lett. **98**, 086801 (2007).

[32] C. Dean, B. Piot, L. Pfeiffer, K. West, and G. Gervais, Physica E **40**, 990 (2008).

[33] C. P. Slichter, *Principles of Magnetic Resonance*, Springer Series in Solid-State Sciences, Springer-Verlag, New York, 3rd edition, 1990.

[34] A. W. Overhauser, Phys. Rev. **92**, 411 (1953).

[35] R. V. Pound, Phys. Rev. **79**, 685 (1950).

[36] C. D. Jeffries, editor, *Dynamic Nuclear Orientation*, Interscience Tracts on Physics and Astronomy, Interscience, 1963.

[37] A. Abragam, J. Combrisson, and I. Solomon, Comptes Rendus Hebdomadaires des Seances de l'Academie des Sciences **247**, 2337 (1958/12/22).

[38] C. D. Jeffries, Phys. Rev. **106**, 164 (1957).

[39] G. Lampel, Phys. Rev. Lett. **20**, 491 (1968).

[40] D. Paget, Phys. Rev. B **24**, 3776 (1981).

[41] D. Paget, G. Lampel, B. Sapoval, and V. I. Safarov, Phys. Rev. B **15**, 5780 (1977).

[42] D. Paget, Phys. Rev. B **25**, 4444 (1982).

[43] E. Hecht, *Optics*, Addison-Wesley, New York, 3rd edition, 1998.

[44] F. Heismann, J. Lightwave Technol. **12**, 690 (1994).

[45] M. Bass, J. M. Enoch, E. Van Stryland, and W. L. Wolfe, editors, *Fiber Optics and Nonlinear Optics*, volume IV of *Handbook of Optics*, J. Opt. Soc. Am., 2000.

[46] A. Yariv, *Optical Electronics in Modern Communications*, Oxford Series in Electrical and Computer Engineering, Oxford University Press, USA, 1997.

[47] R. Ulrich and A. Simon, Applied Optics **18**, 2241 (1979).

[48] R. C. Jones, J. Opt. Soc. Am. **32**, 486 (1942).

[49] T. A. Birks and P. Morkel, Applied Optics **27**, 3107 (1988).

[50] A. Rose, S. Etzel, and C. Wang, J. Lightwave Technol. **15**, 803 (1997).

[51] J. L. Cruz, M. V. Andres, and M. A. Hernandez, Applied Optics **35**, 922 (1996).

[52] P. A. Williams, A. H. Rose, G. W. Day, M. N. Deeter, and T. E. Milner, Applied Optics **30**, 1176 (1991).

[53] A. S. Martinez and R. Maynard, Phys. Rev. B **50**, 3714 (1994).

[54] I. V. Kukushkin, K. von Klitzing, K. Ploog, V. E. Kirpichev, and B. N. Shepel, Phys. Rev. B **40**, 4179 (1989).

[55] M. J. Chou, D. C. Tsui, and G. Weimann, Appl. Phys. Lett. **47**, 609 (1985).

[56] A. S. Chaves and H. Chacham, Appl. Phys. Lett. **66**, 727 (1995).

[57] J. Buset et al., Physica E **40**, 1252 (2008).

[58] A. H. Mack, J. Riordon, C. R. Dean, R. Talbot, and G. Gervais, Opt. Lett. **32**, 1378 (2007).

[59] H. D. M. Davies, J. C. Harris, J. F. Ryan, and A. J. Turberfield, Phys. Rev. Lett. **78**, 4095 (1997).

[60] R. G. Mani et al., Nature **420**, 646 (2002).

[61] A. J. Shields, J. L. Osborne, M. Y. Simmons, D. A. Ritchie, and M. Pepper, Semicond. Sci. Technol. **11**, 890 (1996).

[62] J. H. Davies, *The Physics of Low-dimensional Semiconductors: An Introduction*, Cambridge University Press, New York, 1998.

[63] F. R. Arams, *Infrared to millimeter wavelength detectors*, Dedham, Mass.: Artech House, 1973.

[64] F. J. Low, J. Opt. Soc. Am. **51**, 1300 (1961).

[65] F. J. Low and A. R. Hoffman, Applied Optics **2**, 649 (1963).

[66] R. C. Jones, J. Opt. Soc. Am. **43**, 1 (1953).

[67] W. S. Boyle and J. K. F. Rodgers, J. Opt. Soc. Am. **49**, 66 (1959).

[68] J. C. Mather, Applied Optics **21**, 1125 (1982).